1   **Element release and reaction-induced porosity alteration during shale-hydraulic**

2   **fracturing fluid interactions**

3

4   Anna L. Harrison[a,b*,1], Adam D. Jew[a,b], Megan K. Dustin[a], Dana L. Thomas[a],

5   Claresta M. Joe-Wong[a], John R. Bargar[b], Natalie Johnson[c], Gordon E. Brown Jr.[a,b,c] , and

6   Katharine Maher[a]

7

8   [a]Department of Geological Sciences, 450 Serra Mall, Stanford University, Stanford, CA

9   94305, USA.

10

11   [b]Stanford Synchrotron Radiation Lightsource, SLAC National Accelerator Laboratory,

12   2575 Sand Hill Road, Menlo Park, CA, 94025, USA.

13

14   [c]Department of Photon Science, SLAC National Accelerator Laboratory, 2575 Sand Hill

15   Road, Menlo Park, CA, 94025, USA

16

17   [1]Present address: Department of Earth Sciences, University College London, Gower

18   Street, London, WC1E 6BT, UK. *ALH - anna.harrison@ucl.ac.uk

19

20   *Corresponding author (phone: 1 650 723-2544; facsimile: 1 650 725-2199; e-mail:

21   anna.harrison@ucl.ac.uk).

22

Abstract

The use of hydraulic fracturing techniques to extract oil and gas from low permeability shale reservoirs has increased significantly in recent years. During hydraulic fracturing, large volumes of water, often acidic and oxic, are injected into shale formations. This drives fluid-rock interaction that can release metal contaminants (*e.g.*, U, Pb) and alter the permeability of the rock, impacting the transport and recovery of water, hydrocarbons, and contaminants. To identify the key geochemical processes that occur upon exposure of shales to hydraulic fracturing fluid, we investigated the chemical interaction of hydraulic fracturing fluids with a variety of shales of different mineralogical texture and composition. Batch reactor experiments revealed that the dissolution of both pyrite and carbonate minerals occurred rapidly, releasing metal contaminants and generating porosity. Oxidation of pyrite and aqueous Fe drove precipitation of Fe(III)-(oxy)hydroxides that attenuated the release of these contaminants via co-precipitation and/or adsorption. The precipitation of these (oxy)hydroxides appeared to limit the extent of pyrite reaction. Enhanced removal of metals and contaminants in reactors with higher fluid pH was inferred to reflect increased Fe-(oxy)hydroxide precipitation associated with more rapid aqueous Fe(II) oxidation. The precipitation of both Al- and Fe-bearing phases revealed the potential for the occlusion of pores and fracture apertures, whereas the selective dissolution of calcite generated porosity. These pore-scale alterations of shale texture and the cycling of contaminants indicate that chemical interactions between shales and hydraulic fracturing fluids may exert an important control on the efficiency of hydraulic fracturing operations and the quality of water recovered at the surface.

1. Introduction

The extraction of oil and gas resources from low permeability shale reservoirs has increased dramatically in recent years owing to the development and application of horizontal drilling and hydraulic fracturing techniques (Kerr, 2010; U.S. Energy Information Administration, 2013; Vidic et al., 2013). The development of these resources has dramatically altered the energy landscape, particularly in the United States (Kerr, 2010; U.S Energy Information Administration, 2013), which hosts numerous economically viable shale oil and gas plays (Chermak and Schreiber, 2014; Vengosh et al., 2013). However, hydraulic fracturing operations remain plagued by environmental concerns, namely their potential to impact surface water and groundwater quality (Brantley et al., 2014; Vengosh et al., 2013; Vidic et al., 2013). During hydraulic fracturing operations, large volumes of fracturing fluids (*i.e.*, ~8-17 million liters; Balashov et al., 2015; Chapman et al., 2012), that are often acidic and oxic (Stringfellow et al., 2014), are injected into subsurface shale formations, resulting in a system that is highly out of chemical equilibrium. It is hypothesized that disequilibrium between shale and the hydraulic fracturing fluid will induce a myriad of reactions, including mineral dissolution-precipitation, cation exchange, surface complexation, and oxidation-reduction (redox) of solid and aqueous components. Such reactions may release harmful contaminants into the environment (*e.g.*, U, Ra, As, Pb) (Balaba and Smart, 2012; Blauch et al., 2009; Chermak and Schreiber, 2014; Vengosh et al., 2014; Vidic et al., 2013). These chemical interactions may also alter the permeability and mechanical integrity of the reservoir, influencing the efficiency of production and recovery of water for re-use. Precipitation of secondary minerals and weakening and collapse of fractures due to

3

69   mineral dissolution could in part be responsible for the relatively inefficient production

70   experienced by many hydraulic fracturing operations (U.S. Energy Information

71   Administration, 2013). However, very little is currently known about the extent to which

72   chemical interactions between shales and these introduced fluids alter fluid and rock

73   properties, and whether these interactions occur on a timescale relevant to hydraulic

74   fracturing operations. Although monitoring of so-called flow-back and produced waters

75   (waters generated following fracturing and co-produced with hydrocarbons during well

76   operation, respectively) has revealed that the chemical composition of recovered waters

77   differs substantially from that of the injected fluid, the controls on the evolving

78   composition of the recovered fluids is not fully understood, and may reflect a

79   combination of factors including mixing of injected and formation fluids and fluid-rock

80   interaction (Barbot et al., 2013; Haluszczak et al., 2013; Lester et al., 2015; Orem et al.,

81   2014; Renock et al., 2016; Rowan et al., 2015; Shih et al., 2015; Ziemkiewicz and He,

82   2015; Zolfaghari et al., 2016). Experimental investigation is required to better define the

83   reactions that are likely to occur upon exposure of shales to hydraulic fracturing fluids

84   and their kinetics to assess the potential contribution of fluid-rock interaction to the

85   chemistry of produced waters and alteration of shale mechanical properties.

86   We investigated the types and relative rates of reactions occurring between shales

87   of different chemical and mineralogical compositions and a simulated hydraulic

88   fracturing fluid using a series of batch reactor experiments. Shale samples from four

89   different oil or gas shale reservoirs with unique mineralogical compositions were used,

90   including carbonate mineral-rich rocks from the Eagle Ford (South Texas) and Green

91   River (Colorado) formations, and comparatively carbonate mineral-poor rocks from the

92   Barnett (Central Texas) and Marcellus (New York) formations, all in the United States.

93   Currently, hydrocarbon production via hydraulic fracturing operations is ongoing for the

94   Eagle Ford, Barnett, and Marcellus formations. Green River shale is an oil-bearing

95   formation that, while not presently being exploited, has unique mineralogy that provides

96   an informative contrast to the other shales under investigation. The objectives of this

97   study were to: (1) identify the key geochemical reactions that occur upon exposure of oil

98   or gas-bearing shales to hydraulic fracturing fluids and their kinetics, (2) elucidate the

99   impact of initial shale mineralogy on the evolution of rock and fluid compositions during

100   hydraulic fracturing operations, (3) evaluate the potential for release of metal

101   contaminants to flowback and produced waters, and (4) assess reaction-induced

102   alterations of shale porosity. The evolution of fluid composition was tracked with time,

103   and the physical and chemical alteration of the shales was investigated post-reaction

104   using a combination of x-ray diffraction, x-ray fluorescence spectroscopy, and scanning

105   electron microscopy.

106

107   **2. Methods**

108   *2.1 Experimental methods*

109   The impacts of initial mineralogical composition and texture on the evolution of

110   shale reservoir geochemistry following injection of hydraulic fracturing fluid were

111   investigated using batch reactor experiments. A schematic of the experimental design and

112   further detail regarding experimental methods and analytical techniques are provided in

113   the Supporting Information (SI). Experiments were conducted for three weeks (referred

114   to as "short-term" experiments), three months ("intermediate-term"), and six months

115 ("long-term"). The short-term experiments were representative of the typical duration of

116 fluid injection for hydraulic fracturing, whereas the intermediate- and long-term

117 experiments were designed to investigate the interactions that may occur between the

118 shale reservoirs and unrecovered fracturing fluid over longer timescales after initial

119 fracturing operations are complete. In excess of 50% of the injected hydraulic fracturing

120 fluid is estimated to remain in the subsurface where it may continue to react with the rock

121 (Balashov et al., 2015; Roychaudhuri et al., 2013).

122 All experiments were conducted at Marcellus reservoir-representative

123 temperatures (80°C; Renock et al., 2016; Rowan et al., 2015) and circum-atmospheric

124 pressure in unstirred borosilicate glass serum vials. The use of circum-atmospheric rather

125 than reservoir pressures will cause minor differences in solubility between experimental

126 and field conditions, but the types of minerals that dissolve and their relative rates of

127 dissolution are not expected to be strongly impacted by differences in pressure.

128 Moreover, the impacts of pressure on solubility are small compared to temperature effects

129 (Morel and Herring, 1993). Shale samples from four different oil and/or gas-bearing

130 geological environments representing a wide range of clay and carbonate mineral

131 contents were exposed to simulated hydraulic fracturing fluid (SI Figure S1). These shale

132 samples included the Marcellus (M) gas shale (Oatka Creek Member, New York), the

133 Eagle Ford (EF) oil/gas shale (South Texas), the Barnett (B) gas shale (Central Texas),

134 and the Green River (GR) oil shale (Mahogany Ledge Member, Colorado). The GR and

135 M shales used were outcrop samples collected in August 2015, and July 2016,

136 respectively. EF and B samples were core samples taken at depth (3915 m and 2613 m,

137 respectively).

138   The initial chemical compositions of the shale samples were quantified using x-

139   ray fluorescence spectroscopy (XRF) by Jew et al. (*in press*) for the exact same GR, EF,

140   B, and M samples used in our experiments and are tabulated in Table 1. Semi-

141   quantitative analysis of initial mineralogical compositions was also conducted by Jew et

142   al. (*in press*) using x-ray diffraction (XRD) data (Table 2). Peak identification was

143   accomplished by matching the four most intense diffraction peaks for a given mineral to

144   diffraction patterns in the National Institute of Standards and Technology (NIST)

145   database. Semi-quantitative analysis was conducted by least squares fitting of the

146   diffraction patterns using the NIST diffraction pattern of reference compounds with the

147   software, JADE (Materials Data, 2002). Although these data are semi-quantitative, they

148   are in good agreement with previously reported mineralogical compositions for these

149   shales (Ali and Hascakir, 2015; Chalmers et al., 2012; Chermak and Schreiber, 2014).

150   For the purposes of this study, we separate the shales into "carbonate-rich" or

151   "carbonate-poor" categories depending on their mineralogical and chemical compositions

152   prior to reaction. Carbonate-rich shales contained >50 wt.% carbonate minerals, and

153   carbonate-poor shales contained <15 wt.% carbonate minerals. The Green River and

154   Eagle Ford samples are therefore designated carbonate-rich, and the Barnett and

155   Marcellus samples designated carbonate-poor. The composition of the simulated

156   fracturing fluid used in the experiments was formulated based on fluid compositions

157   typically employed in hydraulic fracturing operations conducted in the Marcellus shale,

158   and mimics that used in the National Energy Technology Laboratory's Marcellus Well E

159   in Greene County, PA ("FracFocus," 2016; Hammack et al., 2014). It contained 99.78

160   wt.% MilliQ distilled, de-ionized water, 0.13 wt.% hydrochloric acid, 0.03 wt.% guar

161   gum, 0.02 wt.% ethylene glycol, 0.02 wt.% kerosene, 0.02 wt.% polyethylene glycol,

162   5.07×10^{-4} wt.% 2-ethylhexanol, and 1.73×10^{-4} wt.% glycol ether. During hydraulic

163   fracturing operations, all additives are not added simultaneously, but follow a specific

164   sequence. The experimental fluid represents a mixture of the relative proportions of these

165   in a single solution. The initial fluid had a pH of 2.0 and was assumed to be at

166   equilibrium with laboratory pO_2 (~0.21 atm), consistent with the injection of surface

167   waters during hydraulic fracturing operations. A major difference between the

168   experimental fluids and field conditions is that fluids in the field tend to have much

169   higher total dissolved solids (TDS). A high TDS fluid was not used in the experiments for

170   a number of reasons. First, high initial concentrations of anions like SO_4^{2-} and cations like

171   Mg and Ca make it difficult to accurately assess changes in aqueous concentrations due

172   to dissolution-precipitation reactions, and to conduct mass balance calculations to assess

173   the cycling of elements in the reactors. Second, a high TDS fluid may itself alter the rate

174   of mineral dissolution-precipitation reactions compared to published rate data from

175   laboratory experiments conducted at more moderate TDS. This complicates the direct

176   assessment of the impact of the hydraulic fracturing fluid additives on these mineral

177   dissolution-precipitation reactions, as deviations from published data could be due to the

178   high TDS rather than the fracture fluid additives. In addition, high TDS complicates the

179   calculation of aqueous speciation. Finally, fracturing fluids are injected into shale

180   formations at a high rate, displacing and diluting pre-existing formation fluids. This is

181   typically followed by "shut-in" of a well for days to months prior to flowback. The

182   critical fracturing fluid-shale reaction time is hours to days. Under such conditions, the

183   chemistry of the fracturing fluid will dominate in fracture spaces, and formation fluids

184   may be less important. Therefore an assessment of direct shale-fracturing fluid reactions

185   is required.

186   Approximately 1 g of shale that had been pulverized to between 150 and 250 μm

187   diameter was used in each reactor, with 200 mL of solution and ~85 mL of gas-filled

188   headspace with the composition of the laboratory atmosphere. Although the reactors were

189   sealed, limited replenishment of O_2 throughout the experimental duration was facilitated

190   through semi-permeable butyl rubber septa and periodic penetration of the septa with a

191   needle during sampling. A control experiment that lacked shale was conducted for each

192   experimental run time. All reactors contained an α-Al_2O_3 chip (< 0.05 g) that was meant

193   to serve as a substrate to facilitate precipitation of secondary phases. However, this

194   substrate was found to be ineffective for this purpose. Fluid samples were taken

195   periodically to track pH and cation and anion concentrations. Concentrations of Mg, Ca,

196   Fe, and Si, were measured using inductively coupled plasma optical emission

197   spectroscopy (ICP-OES). Concentrations of Al, Pb, U, Sr, and Ni were measured using

198   inductively coupled plasma mass spectrometry (ICP-MS), and sulfate concentration was

199   measured using ion chromatography (IC). Solids were collected post-reaction and were

200   stored under vacuum in a desiccator prior to analysis with XRD, and scanning electron

201   microscopy (SEM) coupled with energy-dispersive spectroscopy (EDS). Measurements

202   of iron speciation in fluids and solids in our experiments are beyond the scope of the

203   present study, and are instead presented in detail by Jew et al. (*in press*).

204   *2.2. Speciation calculations*

205   To evaluate the stability of mineral phases in the presence of the fracturing fluid,

206   and the potential for secondary phase formation, speciation calculations were conducted

207   using experimental pH and cation and sulfate concentration data and the geochemical

208   modeling software, PHREEQC V.3 (Parkhurst and Appelo, 2013) with the Lawrence

209   Livermore National Laboratory (LLNL) database. Owing to the dearth of available

210   thermodynamic data to represent the fracture fluid additives, only the additive HCl was

211   included in the models; the organic additives were neglected. Speciation calculations may

212   therefore overestimate the saturation state of mineral phases if significant complexation

213   of inorganic ions with fracture additives or organic complexes native to the shale samples

214   occurred. It should also be noted that speciation calculations assumed equilibrium

215   between aqueous Fe(II) and Fe(III), despite potential kinetic limitations to aqueous Fe(II)

216   oxidation at low pH (Morgan and Lahav, 2007). Due to a lack of dissolved inorganic

217   carbon (DIC) data, DIC concentrations were assumed to reflect primarily carbonate

218   dissolution and were therefore set to balance dissolved Ca concentrations assuming

219   stoichiometric calcite dissolution, as calcite was determined to be the main source of Ca

220   and the most reactive carbonate phase in the samples (refer to section 3.2.3).

221

222   **3. Results and Discussion**

223   Predictions about the effects of the reaction of hydraulic fracturing fluid with

224   shale on contaminant release, fracturing fluid transport, and hydrocarbon recovery

225   requires identification of the types of reactions that will occur as well as their kinetics.

226   However, the complex mineralogy of shales, the commonality of elements between

227   minerals, and the possibility of incongruent dissolution and secondary mineral

228   precipitation confound the direct attribution of aqueous solute concentrations to specific

229   mineral dissolution-precipitation reactions. To address this, we use multiple lines of

230   evidence to determine the mineral dissolution-precipitation reactions that are most likely

231   to occur over the typical timescale of hydraulic fracturing operations (weeks to months)

232   as well as the shale components that govern the evolution of fluid composition and rock

233   porosity and permeability.

234   *3.1 Evolution of fluid composition*

235   *3.1.1. Calcium, magnesium, and pH*

236   Of the major elements initially present in the shales, Ca was released into the

237   fracturing fluid to the greatest extent. In all experiments the release of Ca was initially

238   rapid, before plateauing at reasonably stable values within 48 h (Figure 1a). The steady-

239   state Ca concentrations differed among the four shales and did not correspond directly to

240   the Ca content of the solid phases. The highest aqueous Ca concentration was recorded

241   for the EF shale, followed by the M, the GR, and finally, the B shales (Figure 1a). Yet,

242   the initial solid Ca content of the GR shale exceeded that of the M shale (Table 1). The

243   maximum aqueous Ca values during three weeks of reaction were EF (318 mg L^{-1}), M

244   (242 mg L^{-1}), GR (221 mg L^{-1}), and B (192 mg L^{-1}) (Figure 1a). Aqueous Ca

245   concentrations remained relatively stable in both the intermediate- and long-term

246   experiments (Figure 2a), indicating that the majority of Ca release occurred within 48 h.

247   Different Ca concentrations (up to ~30% different) were observed between duplicate M

248   reactors in both the intermediate- and long-term experiments, which is attributed to

249   mineralogical heterogeneity of the starting solids (Figure 2a). Small differences in Ca

250   concentration trends between the short-term Barnett duplicates are also attributed to

251   heterogeneity of the initial solids. The Marcellus exhibited a large degree of

252   heterogeneity visible at the millimeter scale (SI Figure S2). The smaller degree of

11

253   heterogeneity in the Barnett samples compared to the Marcellus samples is attributed to

254   different sampling protocols; the Barnett was sampled from core, whereas the Marcellus

255   was sampled from outcrop.

256   Trends in Mg release to solution were similar to those observed for Ca for the GR, M,

257   and B shales, with a rapid initial increase within 48 h, followed by relatively stable

258   concentrations for the remainder of the short-term experiments (SI Figure S3). However,

259   maximum aqueous Mg concentrations were lower than Ca solution concentrations, with

260   less than 50 mg L^{-1} Mg for all four shales. This is consistent with the lower solid phase

261   Mg content for all shales (Table 1). Similar to Ca, Mg concentrations remained relatively

262   stable for the durations of the intermediate- and long-term experiments for the GR, M,

263   and B shales, suggesting that the majority of Mg release also occurred within the first 48

264   h of reaction (SI Figure S3). Although Mg content in the initial shale material for EF was

265   similar to B and M (Table 1), the total concentration of Mg in solution was significantly

266   lower (< 3 mg L^{-1}) in the short- and intermediate-term experiments, and remained below

267   quantifiable limits for the long-term experiment (*i.e.*, <1 mg L^{-1}).

268   In all experiments the rapid increases in Ca concentrations within 48 h coincided with

269   rapid increases in solution pH (Figure 1a,b). In fact, two distinct trends in fluid pH were

270   evident in the experiments as a function of the initial carbonate mineral content of the

271   rock. The carbonate-rich EF and GR shales exhibited rapid pH increases from values of

272   ~2 before plateauing at circum-neutral values within 48 h, which coincided with plateaus

273   in Ca concentration (Figure 1b). The pH was maintained at circum-neutral levels

274   throughout the durations of the intermediate- and long-term carbonate-rich shale reactors

275   (Figure 2b). Conversely, the pH for the carbonate-poor B and M reactors remained acidic,

276   plateauing at values between 3 and 5 for experiments of all durations up to six months

277   (Figures 1b and 2b). Differences in fluid pH between duplicate reactors were documented

278   for the intermediate- and long-term M reactors, as was observed for Ca concentrations

279   and was attributed to sample heterogeneity (Figure 2b). The experiments with higher pH

280   corresponded to those with higher Ca concentrations.

281   *3.1.2. Iron release*

282   All Fe concentrations reported represent total aqueous Fe as measured with ICP-OES.

283   Iron concentrations were too low to be quantified using our analytical techniques for the

284   GR and EF shales in reactors of all timescales (<~0.3 ppm). Aqueous Fe concentrations

285   for both the M and B shales, on the other hand, increased rapidly within ~200 h. Fe

286   concentrations reached up to 27 mg L^{-1} in the M reactor and 17 mg L^{-1} in the B reactors,

287   after which Fe concentrations declined for both B and M (Figure 1c). However, Fe

288   concentrations did not decline over time in the intermediate- or long-term B reactors.

289   Rather, they oscillated at ~20 mg L^{-1} for the majority of the intermediate-term reactor and

290   exhibited a gradual increase to 37 mg L^{-1} in the long-term reactor (Figure 2c). As

291   observed for Ca concentrations, duplicate M shale reactors exhibited different Fe

292   concentrations in both the intermediate- and long-term experiments (Figure 2c). Iron

293   concentrations oscillated between 12 and 32 mg L^{-1} in one intermediate-term experiment,

294   but remained below 14 mg L^{-1} in the duplicate experiment. A more pronounced

295   difference was documented for the long-term experiments; the Fe concentration

296   continued to gradually increase throughout the experimental duration in one reactor,

297   reaching up to 37 mg L^{-1}, whereas the Fe concentration was fairly stable between 3 and 6

298   mg L^{-1} for the duplicate experiment (Figure 2c).

299

300   *3.1.3. Sulfate release*

301   Unlike the decline observed for Fe, aqueous SO_4^{2-} concentrations increased

302   throughout the short-term B and M experiments (Figure 1d). Similarly, in the short-term

303   EF experiment, SO_4^{2-} concentrations increased throughout the experimental duration,

304   despite the lack of measurable Fe in solution. In the GR reactors, on the other hand,

305   aqueous SO_4^{2-} concentrations remained below quantifiable values. This is a consequence

306   of the minimal pyrite in this shale. The differences observed for the concentrations of

307   other elements (Ca, Fe) and pH between duplicate M experiments were less pronounced

308   for SO_4^{2-}. The SO_4^{2-} concentrations were similar between duplicate M intermediate-term

309   reactors, and stabilized after 722 h between 134 and 147 mg L^{-1}. In the long-term

310   experiments, SO_4^{2-} concentrations stabilized within 966 h, plateauing at ~140 mg L^{-1} in

311   one reactor and ~170 mg L^{-1} in the other reactor (Figure 2d). A similar extent of sulfate

312   release was observed for the long-term compared to the intermediate-term experiments

313   for all shales, except for the EF, for which a maximum of 98 mg L^{-1} SO_4^{2-} was measured

314   in the intermediate-term compared to 141 mg L^{-1} in the long-term experiment (Figure

315   2d).

316   Pyrite was the only S-bearing phase detected with XRD (Table 2), therefore its

317   release to solution is attributed primarily to pyrite dissolution. Mass balance calculated

318   with respect to the XRF-measured sulfur content of the initial solids and final aqueous

319   SO_4^{2-} concentrations revealed that approximately 38%, 37%, 39%, and 36% of the total

320   initial pyrite mass was oxidized within three weeks of reaction in the EF, M, and

321   duplicate B experiments, respectively (SI Figure S4). The extent of pyrite oxidation

322 remained less than 55% in all intermediate- and long-term EF, M, and B experiments,

323 except for the long-term EF experiment, for which up to 72% of pyrite was calculated to

324 have been reacted (SI Figure S4). In all cases, the majority of pyrite oxidation occurred

325 within the first three weeks of exposure to the simulated fracturing fluid. This result

326 implies that the injection of oxic fracturing fluids will induce oxidative dissolution of

327 pyrite, releasing Fe and SO_4^{2-} into produced waters on a timescale of hours to weeks.

328   *3.1.3. Aluminum and silicon*

329   The experiments were conducted in borosilicate reactors and contained Al_2O_3

330 substrates; these could release Si and Al to solution. The extent of dissolution of these

331 components of the reactors was assessed by comparing Si and Al concentrations in the

332 controls that lacked shale to reactors that contained shale. There was negligible Al and Si

333 release in the short-term controls, confirming that changes in Al and Si concentrations in

334 the short-term experiments are attributable to reaction of shale components. However, in

335 the intermediate- and long-term experiments, Al and Si concentrations in most reactors

336 were not substantially different from those measured in the control experiments.

337 Therefore Si and Al cycling occurring in these experiments due to reaction of the shale

338 components alone cannot be assessed, and further discussion is limited to the short-term

339 experiments.

340   There was very little net mass transfer of Al and Si from the solid to fluid phase in the

341 short-term reactors (Figure 3c). The greatest extent of Si release in the short-term reactors

342 was documented for the GR shale, reaching 16 mg L^{-1}, whereas similar concentrations of

343 <10 mg L^{-1} were documented for the other three shales (Figure 3a). Al was released to the

344 greatest extent from the Marcellus and Barnett shales, but nevertheless remained below 3

345   mg L^{-1} in all short-term reactors (Figure 3b). This is consistent with the known slow

346   dissolution rates of the silicate minerals present in these shales (Palandri and Kharaka,

347   2004).

348

349   *3.2 Identification and kinetics of key reactions*

350   *3.2.1 Iron cycling reactions*

351   The presence of multiple Fe-bearing phases of varying, and often poorly-constrained

352   reactivity in shales (Carroll et al., 2013), and the array of secondary Fe-bearing minerals

353   that can form (*e.g.,* goethite [FeO(OH)], hematite [Fe$_2$O$_3$], amorphous Fe(OH)$_3$; Blowes

354   et al., 1998; Nordstrom, 1982), complicates attribution of the sources of dissolved Fe and

355   the prediction of its fate. The potential sources of dissolved Fe in the four shales include

356   Fe-bearing carbonate minerals (siderite or (Mg-Ca-Fe)$_x$CO$_3$ solid solutions), clays (illite,

357   smecite, and chlorite-group minerals), organic matter, and pyrite. The low extent of Si

358   and Al release in all experiments is consistent with the relatively slow dissolution rates of

359   aluminosilicate minerals compared to carbonate minerals and pyrite (*i.e.,* 10$^{-5.81}$ mol/m^2/s,

360   10$^{-4.55}$ mol/m^2/s, 10$^{-9.12}$ mol/m^2/s, and 10$^{-12.78}$ mol/m^2/s for calcite, pyrite, anorthite, and

361   smecite, respectively, at 25°C and neutral pH; *c.f.,* Palandri and Kharaka, 2004; Golubev

362   et al., 2009; Rimstidt and Vaughan, 2003; Smith et al., 2013), and suggests that the

363   dissolution of clays was not the main contributor of dissolved Fe in the experiments.

364   Rather, the substantial increase in aqueous SO$_4^{2-}$ concentration in all experiments with

365   pyrite-bearing shales (EF, B, and M) indicates that dissolution of pyrite was an important

366   control on Fe release. The GR shale used in the experiments lacked detectable pyrite

367   based on XRD characterization, although minor pyrrhotite [Fe$_{(1-x)}$S] was detected with

16

368   XRF mapping (Jew et al., *in press*), and neither dissolved Fe nor SO_4^{2-} reached

369   quantifiable concentrations in these reactors.

370   Pyrite is interpreted to be the main source of aqueous SO_4^{2-}, therefore deviation of

371   Fe:SO_4^{2-} molar ratios from stoichiometric pyrite values (0.5) are indicative either of

372   secondary phase precipitation, which preferentially removes one element over the other,

373   or dissolution of other Fe-bearing minerals. The Fe concentrations that would be

374   produced from stoichiometric pyrite dissolution based on measured SO_4^{2-} concentrations

375   were calculated for all pyrite-bearing shales (Figures 1c and 2c). Measured Fe

376   concentrations that are less than calculated Fe concentrations are indicative of

377   precipitation of Fe-bearing phases, whereas measured Fe concentrations that are greater

378   than calculated values indicate either precipitation of SO_4^{2-}-bearing phases or an

379   additional source of Fe in the experiments (*e.g.,* siderite dissolution). For M shale, Fe

380   concentrations declined below stoichiometric values after 200 h in the short-term

381   experiments and remained significantly lower (>8 mg L^{-1} lower) than stoichiometric

382   throughout the durations of the intermediate- and long-term experiments (Figures 1c and

383   2c). Similarly, Fe concentrations were below detection for the EF experiments, yet

384   stoichiometric pyrite dissolution would generate up to 26, 28, and 48 mg L^{-1} Fe in the

385   short-, intermediate-, and long-term experiments, based on SO_4^{2-} concentrations. The

386   oxidative dissolution of pyrite is commonly accompanied by precipitation of secondary

387   Fe(III)-bearing (hydr)oxide phases (Blowes et al., 1998; Nordstrom, 1982), and

388   speciation calculations revealed that amorphous Fe(OH)$_3$ became supersaturated in M

389   reactors within 24 h (Figure 4a). Moreover, rust-colored precipitates were observed in

390   suspension and coating the walls of the reactors for both the M and B experiments of all

391   durations, suggesting the presence of oxidized Fe-bearing secondary phases (SI Figure

392   S5). Though the lack of aqueous Fe data for the EF experiments precludes direct

393   calculation of the saturation indices of Fe-bearing minerals, the Fe concentration

394   necessary to saturate the fluid with respect to amorphous $Fe(OH)_3$ in these experiments is

395   sufficiently low such that the solutions may have been saturated with respect to this phase

396   without measurable Fe concentrations. The removal of iron from solution relative to

397   sulfate in both the M and EF experiments is thus inferred to reflect the precipitation of

398   secondary Fe(III)-(oxy)hydroxide phase(s). Similarly, the observation of rust-colored

399   precipitates coating reacted GR particles indicates that Fe(III)-bearing precipitates were

400   also formed in these experiments (SI Figure S5), despite the lack of pyrite. Pyrrhotite was

401   identified with synchrotron-based XRF mapping at low abundance and as the main host

402   of Fe in these samples before reaction (Jew et al., *in press*), suggesting pyrrhotite rather

403   than pyrite dissolution may have been the source of Fe in the GR experiments. Fe(III)-

404   bearing precipitates were not present in sufficient quantities in any of the experiments to
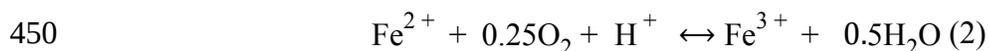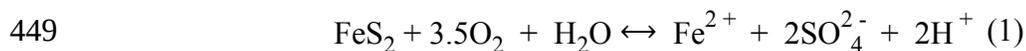
405   identify with XRD.

406   In contrast to the M and EF, the B exhibited greater Fe release than can be attributed

407   to stoichiometric pyrite dissolution within the first 100 h of reaction, and in the

408   intermediate- and long-term B experiments, Fe concentrations remained in excess of

409   those predicted by stoichiometric pyrite dissolution for the majority of the experimental

410   durations (Figures 1c and 2c). The rapid increase in Fe concentration relative to sulfate at

411   the beginning of the experiments implies that a mineral with a rapid dissolution rate, such

412   as siderite or Fe-bearing calcite, was also contributing Fe to solution. This implication

413   could also result in excess Fe concentrations compared to stoichiometric pyrite

414   dissolution in the longer-term experiments. Alternatively, precipitation of S-bearing

415   phases could produce the apparent excess in Fe concentration, and would also serve to

416   clog pore spaces. Speciation calculations revealed that Ca-sulfate minerals were not

417   saturated in the bulk solution, yet precipitates containing Ca, S, and O were identified

418   with SEM and EDS in B samples from the long-term experiments (SI Figures S6 and S7).

419   As such, it is not certain whether these precipitates formed *in situ* during the experiments,

420   or were an artifact formed when the samples were dried following the experiment. If

421   formed during the experiments, these precipitates could account for the excess Fe in

422   solution with respect to stoichiometric pyrite dissolution. However, following the initial

423   rapid release, Fe concentrations in the short-term B experiments declined below

424   stoichiometric values for pyrite dissolution after 95 h (Figure 1c), which is again

425   attributed to the formation of Fe(III)-(oxy)hydroxide. Similarly, the lack of measurable

426   aqueous Fe throughout the EF and GR experiments and the decline in Fe concentration

427   after 95 h in the M experiment implies that precipitation of Fe(III)-(oxy)hydroxides

428   began at least within 95 h in these experiments. This conclusion suggests precipitates

429   could form within hours of hydraulic fracturing and could have significant consequences

430   on the transport and recovery of hydrocarbons and the compositions of flowback and

431   produced waters.

432   *3.2.2. Controls on pyrite oxidation*

433   The dissolution of pyrite from oil and gas shales is of concern, as it is known to

434   release trace metal contaminants, including As, Pb, and Hg (Rimstidt and Vaughan,

435   2003); therefore, it is important to constrain the extent of pyrite reaction that may occur

436   upon injection of oxidized fracturing fluids into shales. In our experiments, the

437   incomplete reaction of pyrite (SI Figure S4) indicates that its dissolution became

438   inhibited over time. There are a number of potential explanations for the apparent

439   inhibition of pyrite dissolution, including: (i) passivation of pyrite surfaces due to

440   precipitation of secondary minerals as surface coatings (Nicholson et al., 1990), (ii)

441   exhaustion of the $O_{2(aq)}$ supply in the reactor, as O_2 is required for oxidative pyrite

442   dissolution, or (iii) pyrite grains located near the surface of the shale particles were

443   consumed at early times, leaving the remaining pyrite within the interior of shale particles

444   poorly exposed to the reactive fluid. This latter possibility is dismissed, as numerous

445   pyrite grains exposed on the surfaces of reacted shale particles were observed with SEM.

446   On the other hand, because the oxidation of pyrite, aqueous Fe(II), and other redox-active

447   components consumes O_2 (Eqs. 1 and 2), the dissolution of pyrite may be self-limiting

448   due to the removal of O_2 as a reactant.

449    $$FeS_2 + 3.5O_2 + H_2O \leftrightarrow Fe^{2+} + 2SO_4^{2-} + 2H^+ \ (1)$$

450    $$Fe^{2+} + 0.25O_2 + H^+ \leftrightarrow Fe^{3+} + 0.5H_2O \ (2)$$

451   Using the initial O_2 content of the reactors as a lower limit to the amount of O_2 available,

452   and assuming the reaction stoichiometry in equations 1 and 2 and no additional O_2-

453   consuming reactions, mass balance calculations reveal that there was sufficient oxygen

454   present to facilitate further pyrite reaction in all experiments, except perhaps one long-

455   term M reactor (SI Figure S4). Moreover, the semi-permeable nature of the butyl rubber

456   stoppers facilitated some replenishment of O_2 from the laboratory air. Conversely, the

457   precipitation of Fe-(oxy)hydroxides was inferred from fluid compositions (section 3.2.1.).

458   This inference implies that the incomplete reaction of pyrite in the experiments is more

459 likely attributable to passivation of the pyrite surface via precipitation of Fe-

460 (oxy)hydroxide phases as surface coatings than to a lack of O_2.

461   Although the availability of O_2 was not limiting for pyrite reaction in the

462 experiments, this may not be the case at field scale during hydraulic fracturing operations

463 due to the highly reducing conditions of shale reservoirs, and the higher rock to O_2 ratio

464 than used in our experiments. For example, during a typical hydraulic fracturing

465 operation in the Marcellus shale, approximately 1.7×10^4 m^3 of oxygenated fracturing

466 fluid may interact with ~1.5×10^7 m^3 of shale (Balashov et al., 2015). Assuming the same

467 pyrite abundance as in the Marcellus experiments and initial equilibrium of the fluid with

468 respect to atmospheric pO$_2$, these estimates imply a dissolved O_2 to pyrite molar ratio of

469 3.7×10^{-7}, which is far less than that required to completely oxidize the pyrite (*i.e.*, a ratio

470 of 3.5; Eq. 1). Only 1.0×10^{-5}% of the pyrite would be oxidized under this scenario,

471 implying a similarly low percentage of release of trace metals via its dissolution, if

472 dissolution were to occur stoichiometrically. This suggests that at the scale of typical

473 hydraulic fracturing operations, the amount of pyrite oxidation that can occur will be

474 limited by the O_2 supply when the fluid is imbibed into the matrix. If the fluid is not

475 imbibed to a great extent, the reaction may occur mainly at the fracture-matrix interface,

476 where the supply of O_2 could still be excessive. Similarly at grain scale, the precipitation

477 of Fe-(oxy)hydroxides as surface coatings on pyrite may severely limit the reaction rate

478 of individual pyrite grains, effectively stopping pyrite oxidation. In either case, the

479 magnitude of release of contaminants such as Pb from pyrite dissolution will be governed

480 in part by the amount of oxygen injected into the subsurface, which is a function of the

481 concentration of dissolved oxygen in and the volume of the fracturing fluid injected, and

482   the degree to which this fluid is imbibed into the matrix. The rock:fluid ratios are high in

483   the subsurface, thus even the reaction of a small proportion of reactive phases like pyrite

484   at the fracture-fluid interface may strongly alter the fluid composition.

485   *3.2.3. Dissolution of carbonate minerals*

486   There are a number of minerals in all of the shales that could dissolve to release Ca

487   and Mg to solution, including the carbonate minerals calcite [$CaCO_3$] and dolomite

488   [$Ca,Mg(CO_3)_2$], illite, smectite, and chlorite-group clay minerals, and plagioclase feldspar

489   (Ca-endmember anorthite [$CaAl_2Si_2O_8$]). Dissolution of carbonate minerals is rapid

490   compared to dissolution of aluminosilicate minerals, and calcite dissolution in particular

491   is rapid compared to dolomite dissolution (Palandri and Kharaka, 2004; Pokrovsky et al.,

492   2005). The relatively low degree of Si and Al release in these experiments compared to

493   Ca is consistent with the large differences in dissolution rates of Ca-bearing minerals, and

494   implies that aluminosilicates were not the primary source of dissolved Ca in these

495   experiments. Dissolution of carbonate minerals, on the other hand, is rapid and provides

496   alkalinity to solution. Thus, the coincidence of rapid Ca release rates and rapid pH

497   increases are consistent with Ca-carbonate mineral dissolution as the main source of

498   dissolved Ca in these experiments. Analysis of the shales following reaction with XRD

499   confirmed a reduction of calcite content in all shales, whereas the abundances of dolomite

500   and clays were less altered (Jew et al., *in press*). We conclude that calcite dissolution was

501   the primary source of dissolved Ca for both carbonate-poor and carbonate-rich shales.

502   However, the occurrence of plateaus in Ca concentration and the magnitude of Ca

503   concentration at these plateaus are attributed to different factors for the carbonate-rich

504   compared to the carbonate-poor shales.

505   Speciation calculations revealed that coincident Ca concentration and circum-neutral

506   pH plateaus for the carbonate-rich shales (EF and GR) are associated with achievement of

507   equilibrium with respect to calcite (Figure 5); the fluid reached saturation with respect to

508   calcite within 48 h and remained approximately at equilibrium throughout the remainder

509   of the short-term experiments. Similarly, throughout the intermediate- and long-term EF

510   and GR experiments, fluids remained approximately at equilibrium with respect to

511   calcite. In contrast, for the carbonate-poor B and M shales, the solutions remained

512   undersaturated with respect to calcite for experiments of all durations (Figure 5). Mass

513   balance calculations based on bulk XRF analysis of the initial materials and final aqueous

514   Ca concentrations revealed that these carbonate-poor shales were almost completely

515   stripped of Ca within three weeks, whereas the carbonate-rich EF and GR shales

516   maintained more than 70% of their initial Ca over the same time period (inset Figure 1a).

517   The plateaus in Ca concentration and pH are attributed to the exhaustion of the accessible

518   calcite for the carbonate-poor shales, and to the achievement of equilibrium with respect

519   to calcite for the carbonate-rich shales. The magnitude of the Ca concentration at these

520   plateaus is therefore dictated by the mass of fluid-accessible calcite for the carbonate-

521   poor shales, and the extent of dissolution required to achieve equilibrium for the

522   carbonate-rich shales. The concentration of Ca and fluid pH at equilibrium with respect to

523   calcite will differ slightly between the experiments and field conditions due to the lower

524   pressure used in the experiments.

525   Calcite dissolution generates alkalinity, yet the oxidative dissolution of pyrite

526   generates acidity. Both reactions were documented to occur on a similar timescale in all

527   experiments with pyrite-bearing shales. The pH of the fluid at which the pH values

528   plateau therefore reflects the balance between the extent of pyrite dissolution and the

529   abundance of calcite available to the buffer the fluid pH. In the case of the carbonate-poor

530   shales (B and M), fluids remained acidic as there was insufficient calcite available to

531   counterbalance the combined acidity of the initial fracturing fluid and that generated from

532   pyrite oxidation. Conversely, the carbonate-rich EF and GR shales had sufficient

533   alkalinity-generating capacity to neutralize all acidity. The extent of calcite dissolution

534   that occurs in a shale formation will therefore depend on the initial pH and volume of the

535   injected fluid, as well as the abundance of pyrite in the shale and amount of dissolved

536   oxygen in the injected fluids.

537   Notably, dolomite, another fairly abundant carbonate mineral in these shales (Table

538   2), remained undersaturated in the B and M experiments, was close to equilibrium in the

539   short- and intermediate-term EF experiments, and was slightly supersaturated in the GR

540   experiments (SI Figure S8). The saturation state of siderite [$FeCO_3$] could not be

541   calculated for the EF and GR experiments due to the lack of aqueous Fe concentration

542   data, but it remained undersaturated in the B and M experiments. This finding implies

543   that although dissolution of these other carbonate minerals likely occurred, calcite exerted

544   the strongest control on overall fluid pH and Ca concentrations. The low Mg

545   concentrations documented in the EF shale experiments indicate little dolomite

546   dissolution occurred, despite the solutions approaching equilibrium with respect to

547   dolomite. The similar temporal trends in aqueous Mg compared to Ca indicate it was

548   likely sourced from the dissolution of Mg-bearing calcite for the B and M shales.

549

550

551   *3.3 Alteration of porosity*

552   *3.3.1. Porosity generation*

553   Discrete holes of size similar to intact calcite grains in unreacted material (10s of

554   microns) were observed post-reaction in the B shale for all experimental durations

555   (Figure 6). These holes are attributed to the preferential dissolution of calcite. The

556   generation of large, isolated pores was not observed for the M shale, despite the removal

557   of the majority of the calcite from this shale (Figure 6). This result is attributed to

558   differences in initial calcite distribution and size between the two carbonate-poor shales;

559   the calcite in the M was distributed as clusters of smaller grains (<10 µm), compared to

560   generally larger (~15-50 µm), isolated grains in the B (SI Figures S9 and S10). In the EF

561   shale, calcite was also generally distributed as large, isolated grains (SI Figure S11).

562   Changes in surface morphology of the EF were not broadly evident, but some particles

563   did exhibit a mottled texture indicative of porosity generation (Figure 6).

564   Unlike the other shales, calcite was distributed as pervasive cement that filled the

565   areas between silicate and dolomite grains in the GR shale (SI Figure S12). The

566   preferential dissolution of this calcite cement generated a mottled, spongy texture over

567   the majority of the GR shale surface, consistent with the generation of a porosity network

568   (Figure 6). We inferred from aqueous compositions that ~30% of the calcite was lost

569   from the GR shale. Assuming uniform reaction, this translates to a reaction front

570   penetrating ~42 µm deep in each GR particle, and approximately a 1.5-fold increase in

571   the total estimated bulk pore volume of the particles (initial porosity estimated at 10%;

572   Law et al., 1986). Although the secondary porosity network did not appear to be as

573   uniform in the other shales, the calculated bulk pore volume increase for the entire shale

574   mass of each type was similar. The increase in bulk pore volume was estimated to be 3.0-

575   , 2.2-, and 3.4-fold for the B, EF, and M shales, respectively, based on mass balance

576   estimates of calcite loss, and initial porosity values of 3%, 9%, and 4%, respectively

577   (Chalmers et al., 2012; Jennings and Antia, 2013; Law et al., 1986).

578   Our experiments reveal that the interaction of the calcite-bearing shales with acidic

579   fracturing fluid will generate porosity due to calcite dissolution, but the connectivity and

580   distribution of this porosity is dictated by the pore-scale distribution of calcite. Isolated

581   calcite grains tended to generate discrete pores, whereas more homogeneous calcite

582   distribution appeared to result in a more pervasive secondary porosity network. It is well

583   known that even minor changes in porosity can profoundly influence the permeability of

584   a rock (Andreani et al., 2009; Gouze and Luquot, 2011; Luquot et al., 2012; Luquot and

585   Gouze, 2009; Smith et al., 2013), but the net effect of the generated porosity on fluid

586   transport in these shales requires further investigation. It is possible that secondary

587   porosity could enhance the transport of hydrocarbons across the matrix-fracture interface

588   by increasing permeability. Alternatively, hydrocarbon and fluid transport could be

589   inhibited due to capillary effects or weakening of the shale matrix and the subsequent

590   collapse of fractures and large pores. The higher pressure in shale formations compared

591   to our experiments is likely to exert a strong control on the importance of these porosity-

592   altering reactions on permeability, and the imbibition of the fluid into the matrix, which

593   requires further investigation. The manner in which permeability evolves under stress is

594   impacted by shale mineralogy; clay-rich shales tend to exhibit greater pore-throat

595   compressibility (Al Ismail and Zoback, 2016). Therefore the observed geochemical

596   reactions may alter the response of shale permeability to the stresses experienced during

597   hydraulic fracturing due to changes in composition and distribution of pore types and

598   sizes. Regardless, our experiments reveal that geochemical reactions have the potential to

599   alter porosity, and the manner in which it is altered will depend not only on the

600   abundance, but also on the distribution of highly reactive phases such as calcite.

601

602   *3.3.2. Porosity occlusion*

603   *3.3.2.1 Fe(III)-bearing precipitates*

604   Pyrite is the main source of aqueous Fe and SO_4^{2-} from the M and EF shales, thus

605   the deficit between measured Fe concentrations and those expected for stoichiometric

606   pyrite dissolution can be used to approximate the volume of Fe-(oxy)hydroxide

607   precipitated. In the B experiments, an additional source of Fe precludes simple mass

608   balance calculation. In the case of the M and EF, the main reaction product is inferred to

609   be amorphous $Fe(OH)_3$ in the short-term experiments. Assuming a density of ferrihydrite

610   (3.96 g/cm^3; Jambor and Dutrizac, 1998), the volume of $Fe(OH)_3$ precipitated is only

611   ~4% and 6% of the pore volume generated via calcite dissolution for the EF and M

612   shales, respectively. Despite the reddish coloration observed in the reactors, Fe-

613   (oxy)hydroxides were not observed with SEM, which is consistent with the calculated

614   low volume of precipitates. Thus, calcite dissolution appears to have more strongly

615   influenced the evolution of porosity than did precipitation of secondary phases.

616   Nevertheless, depending on the location in which precipitates form, for example in pore

617   throats versus large pores, they may exert an important control on the transport properties

618   of the rock even with a small volume precipitated (Andreani et al., 2009; Gouze and

619   Luquot, 2011; Luquot et al., 2012; Luquot and Gouze, 2009; Smith et al., 2013). The

620   formation of Fe(III)-precipitates requires the oxidation of both pyrite and aqueous Fe(II),

621   and therefore the total volume of precipitates that can form will be limited by the amount

622   of oxidizing agents that are injected, particularly dissolved O_2.

623   Although the majority of pyrite oxidation concluded within three weeks, speciation

624   calculations revealed that the type of Fe(III)-bearing precipitate may have changed over

625   time during the intermediate- and long-term experiments, as is consistent with known

626   stability of Fe(III)-(oxy)hydroxides (Cudennec and Lecerf, 2006; Schwertmann et al.,

627   1999). The morphology, size, and density of the precipitates are expected to evolve

628   during these phase transformations (Johnston and Lewis, 1983; Michel et al., 2010),

629   therefore porosity and permeability may have continued to evolve due to these

630   transformations. The crystalline phases hematite and goethite were highly supersaturated

631   during the early stages of the reaction for both the M and B shales, whereas the saturation

632   index of amorphous $Fe(OH)_3$ declined towards equilibrium in the short-term experiments.

633   However, in the intermediate- and long-term B experiments, the fluids were

634   undersaturated with respect to amorphous $Fe(OH)_3$, yet close to equilibrium with respect

635   to hematite and goethite (Figure 4). The same was true for duplicate intermediate-term

636   and one of the long-term M experiments. The other long-term M reactor remained close

637   to equilibrium with respect to amorphous $Fe(OH)_3$ due to the higher pH of this reactor

638   compared to its duplicate (data not plotted). The transition from saturation with respect to

639   amorphous $Fe(OH)_3$ to the more crystalline Fe(III)-bearing phases suggests that the

640   poorly crystalline precursors may have been replaced by more stable phases over time

641   (Steefel and Van Cappellen, 1990). Although saturation indices may have been

642   overestimated due to relatively slow aqueous Fe(II) oxidation rates (*i.e.,* not equilibrium),

643   and complexation with organics in the fracture fluid or native to the shale that were not

644   accounted for in the speciation calculations, phase transitions are nevertheless expected in

645   the Fe(III)-(oxy)hydroxide system (Cudennec and Lecerf, 2006; Schwertmann et al.,

646   1999). The reduction in porosity of a reaction layer during similar phase transformations

647   between hydrated Mg-carbonate minerals has been postulated to severely limit reaction

648   rates of dissolving minerals (Harrison et al., 2016, 2015). Though not directly observed in

649   the present study, it is possible that the ripening of secondary phases in the shale-

650   hydraulic fracturing fluid system results in continued porosity and permeability evolution

651   over the longer term even after cessation of pyrite oxidation.

652   *3.3.2.2. Al-bearing precipitates*

653   Colorless, gelatinous suspended solids were observed within 6 h in all of our short-

654   term experiments, including controls, and persisted throughout the intermediate- and

655   long-term experiments. These solids were not successfully recovered from the short-term

656   experiments but were selectively removed at the conclusion of the intermediate- and

657   long-term experiments. Precipitates associated with this gelatinous substance consistently

658   appeared as bulbous, pseudo-spherical entities as observed using SEM (SI Figure S6).

659   EDS analysis indicated that these precipitates are composed of Al, O, and in some cases,

660   Cl, suggesting that they are a poorly-crystalline Al-hydr(oxide) phase (SI Figure S6).

661   Speciation calculations revealed that the Al-hydroxide phases gibbsite [$Al(OH)_3$] and

662   boehmite [γ-AlO(OH)] became supersaturated within 100 h in all short-term experiments

663   (SI Figure S13). The relatively constant level of supersaturation achieved with respect to

664   these phases in the short-term experiments suggests the aqueous Al concentrations were

665   controlled by precipitation of an amorphous Al-hydr(oxide) phase, which is consistent

666　　with the observation of amorphous Al-hydroxide flocs that form during mixing of acidic

667　　mine drainage waters with neutral surface waters (Furrer et al., 2002). The presence of

668　　these Al-bearing precipitates in the short-term experiments could account for the

669　　measured solution compositions, though their presence could not be confirmed with

670　　SEM. Like the Fe(III)-(oxy)hydroxides, these Al-hydr(oxides) provide the potential to

671　　clog pore space and fracture apertures, as well as acting as surfaces for adsorption of

672　　trace metals, should they form in the subsurface. However, both boehmite and gibbsite

673　　were undersaturated in the long-term experiments for all shales, suggesting that they may

674　　not be stable for long durations.

675

676　　*3.4 Contaminant and trace element release*

677　　　*3.4.1 Lead, uranium, and nickel*

678　　　One of the major environmental concerns of hydraulic fracturing operations is the

679　　potential to contaminate ground or surface waters with toxic or radioactive metals such as

680　　As, Pb, and U initially present in the host rock reservoir (Chermak and Schreiber, 2014;

681　　Phan et al., 2015; Vengosh et al., 2014). Such contaminants can be released along with

682　　other trace elements during dissolution of shale minerals and degradation of organic

683　　matter (Jin et al., 2013; Jung et al., 2013; Phan et al., 2015; Tuttle et al., 2009; Wang et

684　　al., 2015). To assess the source and fate of contaminant metals in our shale-fracturing

685　　fluid experiments, the concentrations of U, Pb, and Ni were tracked with time. Lead is a

686　　common trace element in pyrite that can be released upon its dissolution (Rimstidt and

687　　Vaughan, 2003), whereas U in the Marcellus shale is primarily hosted in silicate

688　　minerals, with up to 20% hosted in carbonate minerals (Phan et al., 2015). Aqueous

689 concentrations of both Pb and U remained too low for accurate measurement for all but

690 the M shale. Nickel is a common minor element in pyrite (Rimstidt and Vaughan, 2003)

691 that was present at higher abundance than U and Pb in the shales we examined (Table 1).

692 Nickel concentrations were therefore tracked to provide insight as to the behavior of the

693 typical pyrite-bound contaminants that were not successfully measured for the EF and B

694 shales.

695   Nickel release from the M and B shales exhibited behavior similar to that of SO_4^{2-} in

696 the short-term experiments, and there was negligible Ni release from the GR shale. These

697 trends are consistent with Ni being sourced primarily from pyrite dissolution (Figure

698 7a,b). Declines in Ni concentration were observed in the intermediate- and long-term EF

699 experiments, and remained relatively stable throughout the durations of the intermediate-

700 and long-term B experiments (Figure 7a). Nickel concentrations also exhibited moderate

701 declines in the intermediate- and long-term M experiments, and the maximum

702 concentrations differed between duplicate reactors, as was documented for Ca, Fe, and

703 pH (Figure 7b).

704   Similar to Ni, the temporal trend in aqueous Pb concentration mimicked that of SO_4^{2-}

705 in the short-term M experiments, implying that Pb was also released from dissolving

706 pyrite (Figure 7c). Conversely, U was released rapidly from the M shale in the first 24 h,

707 after which its concentration continued to increase at a much slower rate, reaching a

708 maximum of 64 μg L^{-1} in the short-term experiments (Figure 7d). This result for U is

709 similar to the behavior of Ca and fluid pH, implying that U is primarily sourced from

710 carbonate dissolution, which is consistent with observations of Phan et al. (2015).

711 However, both U and Pb concentrations exhibited pronounced declines over time in one

712   each of the duplicate intermediate- and long-term M experiments (Figures 7c,d). In the

713   other duplicate reactors, U, and Pb concentrations remained significantly lower

714   throughout the experimental durations (Figure 7d). The reactors with low aqueous

715   concentrations of U, Pb, and Ni were also those for which aqueous Ca concentrations and

716   pH were high, but Fe concentrations were low. A comparison of maximum U, Pb, and Ni

717   concentrations versus maximum fluid pH for the M reactors of all durations reveals a

718   tendency of lower U, Pb, and Ni concentration with higher pH (Figure 8a). Sulfate release

719   occurred to a similar magnitude in both intermediate-term M duplicates, and sulfate

720   concentrations were higher in the long-term duplicate experiment with lower Ni, U, and

721   Pb concentrations, indicating that the lower aqueous concentrations of these trace

722   elements cannot be attributed to less pyrite dissolution. Rather, like the concentrations of

723   these trace elements, a tendency toward lower aqueous Fe:S molar ratio as a function of

724   pH was observed in the M reactors (Figure 8b), which is indicative of a greater extent of

725   Fe-(oxy)hydroxide precipitation in the reactors with higher pH. The removal of U, Pb,

726   and Ni from solution likely reflects adsorption at the surface of and/or co-precipitation

727   with these secondary (oxy)hydroxide phases, a well-known phenomenon (Bargar et al.,

728   1997; Benjamin and Leckie, 1981; Bruno et al., 1995; Duff et al., 2002; Enid Martinez

729   and Mcbride, 1998). This greater degree of Fe-(oxy)hydroxide precipitation is facilitated

730   by a faster rate of aqueous Fe(II) oxidation, which increases as a function of pH (Morgan

731   and Lahav, 2007; Stumm and Lee, 1961), and resulted in lower aqueous concentrations of

732   trace metals for the M reactors. A similar process could account for the decline in Ni

733   concentrations in the EF reactors, implying that trace metal contaminants may also be

734   removed in this fashion for the EF shale. The stabilization of Ni concentrations in the

735 longer-term experiments for the B and GR shales may indicate the cessation of

736 dissolution of the source phase for Ni; therefore, it is not clear whether sequestration of

737 trace metals was occurring in these experiments.

738 Although the formation of precipitates may serve to clog porosity and inhibit

739 hydrocarbon recovery, they may also be beneficial due to the apparent mitigation of

740 contaminant release. However, the transformation from less to more stable phases over

741 time may affect the sorption capacity of the secondary phases, therefore contaminant

742 concentrations may continue to evolve along with porosity. As both the precipitation of

743 (oxy)hydroxides and the subsequent sorption of metals are favored at higher pH,

744 contaminant mobility will be highly sensitive to the relative proportion of acid and

745 alkalinity-generating reactants – namely the abundance of calcite and pyrite in the shale,

746 and the concentration of dissolved O_2 and acidic additives present in the fracturing fluid.

747 Higher acid concentrations and lower carbonate mineral content will tend to favor

748 mobility of contaminants. These results imply that the contamination of flowback and

749 produced waters will depend not only on the abundance of contaminants in a given shale

750 formation, but on the relative abundance of acidity- and alkalinity-generating minerals.

751 The composition of hydraulic fracturing fluid should be tailored according to shale

752 mineralogy. For example, a more acidic fluid could be used with carbonate-rich shales

753 while still permitting high pH conditions in the formation.

754 *3.4.2. Strontium release*

755 Trace metals such as Sr, which is commonly substituted in carbonate minerals

756 (Tesoriero and Pankow, 1996), can be used as tracers of fluid-rock interaction that help

757 identify sources of flowback and produced waters (Capo et al., 2014; Chapman et al.,

758   2012; Phan et al., 2016). Strontium concentrations were tracked over time in the

759   experiments to assess the degree to which mineral dissolution may control Sr

760   concentrations and isotopic compositions in the subsurface. Strontium exhibited an

761   initially rapid release for all shales in the short-term experiments and plateaued at

762   relatively constant values for the majority of the intermediate- and long-term

763   experiments, comparable to the behavior observed for Ca and Mg (Figure 9). The release

764   of Sr is primarily attributed to the dissolution of carbonate minerals, particularly calcite,

765   as has been observed during reaction of the Gothic shale with brine and CO_2, and was

766   inferred to occur during hydraulic fracturing fluid interaction with Marcellus shale at

767   field scale (Jung et al., 2013; Stewart et al., 2015). Similar to the release of U and Pb, the

768   extent of release of Sr under field conditions will therefore depend primarily on the

769   balance between acidity- and alkalinity-generating reactions and the ensuing extent of

770   carbonate mineral dissolution. The rapid dissolution rate of calcite upon contact with the

771   fracturing fluid highlights that the release of Sr from carbonate minerals in the shale

772   formations must be considered when Sr isotopic compositions of produced waters are

773   used to determine the sources and flow paths of these waters. If the Sr isotopic

774   composition of the carbonate in the shale formation is known, the Sr isotopic composition

775   of the fluid can also be used to help constrain the extent of fluid-rock interaction incurred

776   in the fractured formation.

777

778   **4. Summary and implications for hydraulic fracturing operations**

779   Our experiments revealed that exposure of shales to hydraulic fracturing fluid can

780   induce an array of reactions independent of the exact composition of the shale. The

781   mineralogy of the shale, along with the distribution of the minerals, will strongly dictate

782   the evolution of fluid composition. The simulated fracturing fluid in our experiments

783   prompted extensive dissolution of calcite and pyrite, and minor dissolution of silicate

784   minerals in all shales containing these minerals. The dissolution of calcite tended to

785   generate porosity, which could serve either to enhance hydrocarbon transport, or may

786   lead to weakening of the shale matrix and collapse of fractures. On the other hand, the

787   formation of secondary (oxy)hydroxide phases will clog pore spaces and may block

788   fracture apertures, a process that may contribute to the field-observed inefficient recovery

789   of hydrocarbons. Mineral dissolution reactions released trace metal contaminants to

790   solution that could be brought to the surface with produced and flowback waters,

791   incurring the risk of contaminating surface waters and necessitating treatment of

792   produced waters for safe disposal or re-use (Vengosh et al., 2013, 2014). However, the

793   precipitates were inferred to remove the contaminants from solution via adsorption and/or

794   co-precipitation, which could partially mitigate contaminant transport in the subsurface.

795   Mineral dissolution-precipitation reactions, rates of aqueous Fe(II) oxidation, and

796   sorption of contaminants are highly sensitive to fluid pH, which was found to be

797   governed most strongly by the mineralogical composition of the rock. Carbonate-rich

798   shales rapidly recovered fluid pH to circum-neutral conditions, whereas fluids in contact

799   with carbonate-poor shales remained acidic. More extensive calcite dissolution generated

800   higher pH, and permitted an apparently greater extent of Fe-(oxy)hydroxide precipitation

801   and more efficient removal of metal contaminants from solution. The implication is that

802   both reaction-induced porosity alteration and the release of contaminants will depend

803   strongly on the volume of fluid injected, as well as the acidity of the fluid and the

804   dissolved oxygen content. Moreover, the mineralogical composition and pore-scale

805   distribution of highly reactive phases, such as pyrite and calcite, will dictate the degree to

806   which contaminants are released and the manner in which porosity develops, as will the

807   effective rock volume with which the fluid reacts (*i.e.*, the degree of imbibition). Further

808   investigation is required to better understand the physical controls on fluid uptake into the

809   matrix and thus the extent of reaction that may occur. In any case, our experiments reveal

810   that both the release of contaminants and formation of porosity-clogging precipitates

811   could be minimized by utilizing fracturing fluids with lower dissolved oxygen content.

812   Although fracturing fluids often include complexing agents designed to inhibit

813   precipitation of secondary phases to minimize mineral scale formation, our experimental

814   results suggest that this practice may counteract the beneficial removal of metal

815   contaminants from solution in the presence of O_2. Overall, our experiments illustrate that

816   fracture fluid compositions and residence times should be adjusted according to shale

817   mineralogy. In carbonate-rich reservoirs, more rapid flushing of fluids, higher acid

818   concentrations, or higher concentrations of Fe-complexing agents would be required

819   compared to carbonate-poor reservoirs to reduce mineral precipitation. In carbonate-poor

820   reservoirs, on the other hand, the low fluid pH may facilitate greater release of metal

821   contaminants (*e.g.*, U, Pb), and therefore more treatment and monitoring of flowback and

822   produced waters may be required. It should also be noted that formation waters typically

823   contain much higher total dissolved solids then were used in our experiments. This

824   difference in initial fluid chemistry may impact some of the reactions observed in our

825   experiments, such as the saturation state of secondary minerals, and the sorption behavior

826   of trace metals. The impacts of high total dissolved solids therefore require further

827 investigation, although the degree to which these fluids may be displaced and diluted, and

828 therefore continue to react within the fractured zone is unknown. Our experiments

829 confirm that a number of reactions can be induced between shales and fluids containing

830 the typical fracturing fluid additives, highlighting the need to better understand these

831 interactions over a variety of geochemical conditions.

832

833 **Supporting Information**

834 A detailed description of the experimental design, analytical methods, speciation

835 calculation results, and supplementary data are available in the Supporting Information.

836

837 **Acknowledgments**

850   **References**

851   Al Ismail, M.I., Zoback, M.D., 2016. Effects of rock mineralogy and pore structure on

852   extremely low stress-dependent matrix permeability of unconventional shale gas and

853   shale oil samples. Phil. Trans. R. Soc. A. 374, DOI: 10.1098/rsta.2015.0428.

854   Ali, M., Hascakir, B., 2015. Water-Rock Interaction for Eagle Ford, Marcellus, Green

855   River, and Barnett. SPE East. Reg. Meet. 1–16.

856   Andreani, M., Luquot, L., Gouze, P., Godard, M., Hoisé, E., Gibert, B., 2009.

857   Experimental study of carbon sequestration reactions controlled by the percolation

858   of CO_2-rich brine through peridotites. Environ. Sci. Technol. 43, 1226–1231.

859   Balaba, R.S., Smart, R.B., 2012. Total arsenic and selenium analysis in Marcellus shale,

860   high-salinity water, and hydrofracture flowback wastewater. Chemosphere 89,

861   1437–1442.

862   Balashov, V.N., Engelder, T., Gu, X., Fantle, M.S., Brantley, S.L., 2015. A model

863   describing flowback chemistry changes with time after Marcellus Shale hydraulic

864   fracturing. Am. Assoc. Pet. Geol. Bull. 99, 143–154.

865   Barbot, E., Vidic, N., Gregory, K., Vidic, R., 2013. Spatial and temporal correlation of

866   water quality parameters of produced waters from devonian-age shale follwoing

867   hydraulic fracturing. Environ. Sci. Technol. 47, 2562–2569.

868   Bargar, J.R., Brown, G.E., Parks, G.A., 1997. Surface complexation of Pb(II) at oxide-

869   water interfaces: II. XAFS and bond-valence determination of mononuclear Pb(II)

870   sorption products and surface functional groups on iron oxides. Geochim.

871   Cosmochim. Acta 61, 2652–2652.

872   Benjamin, M.M., Leckie, J.O., 1981. Multiple-site adsorption of Cd, Cu, and Pb on

873   amorphous iron oxyhydroxides. J. Colloid Interface Sci. 79, 209–221.

874 Blauch, M.E., Myers, R.R., Moore, T.R., Lipinski, B.A., Houston, N.A., 2009. Marcellus

875   shale post-frac flowback waters - where is all the salt coming from and what are the

876   implications?, *in*: Society of Petroleum Engineers, Eastern Regional Meeting:

877   Charleston, WV, September 23-25.

878 Blowes, D.W., Jambor, J.L., Hanton-fong, C.J., Lortie, L., Gould, W.D., 1998.

879   Geochemical , mineralogical and microbiological characterization of a sulphide-

880   bearing carbonate-rich gold-mine tailings impoundment, Joutel, Quebec. Appl.

881   Geochem. 13, 687–705.

882 Brantley, S.L., Yoxtheimer, D., Arjmand, S., Grieve, P., Vidic, R., Pollak, J., Llewellyn,

883   G.T., Abad, J., Simon, C., 2014. Water resource impacts during unconventional

884   shale gas development: The Pennsylvania experience. Int. J. Coal Geol. 126, 140–

885   156.

886 Bruno, J., De Pablo, J., Duro, L., Figuerola, E., 1995. Experimental study and modeling

887   of the U(VI)-Fe(OH)$_3$ surface precipitation/coprecipitation equilibria. Geochim.

888   Cosmochim. Acta 59, 4113–4123.

889 Capo, R.C., Stewart, B.W., Rowan, E.R., Kohl, C.A.K., Wall, A.J., Chapman, E.C.,

890   Hammack, R.W., Schroeder, K.T., 2014. The strontium isotopic evolution of

891   Marcellus formation produced waters, southwestern Pennsylvania. Int. J. Coal

892   Geol. 126, 57–63.

893 Carroll, S.A., McNab, W.W., Dai, Z., Torres, S.C., 2013. Reactivity of Mount Simon

894   Sandstone and the Eau Claire Shale under CO_2 storage conditions. Environ. Sci.

895   Technol. 47, 252–261.

896   Chalmers, G.R., Bustin, R.M., Power, I.M., 2012. Characterization of gas shale pore

897   systems by porosimetry, pycnometry, surface area, and field emission scanning

898   electron microscopy/transmission electron microscopy image analyses: Examples

899   from the Barnett, Woodford, Haynesville, Marcellus, and Doig units. Am. Assoc.

900   Pet. Geol. Bull. 96, 1099–1119.

901   Chapman, E.C., Capo, R.C., Stewart, B.W., Kirby, C.S., Hammack, R.W., 2012.

902   Geochemical and strontium isotope characterization of produced waters from

903   Marcellus shale natural gas extraction. Environ. Sci. Technol. 6, 3545–3553.

904   Chermak, J.A., Schreiber, M.E., 2014. Mineralogy and trace element geochemistry of gas

905   shales in the United States: Environmental implications. Int. J. Coal Geol. 126, 32–

906   44.

907   Cudennec, Y., Lecerf, A., 2006. The transformation of ferrihydrite into goethite or

908   hematite, revisited. J. Solid State Chem. 179, 716–722.

909   Duff, M.C., Coughlin, J.U., Hunter, D.B., 2002. Uranium co-precipitation with iron oxide

910   minerals. Geochim. Cosmochim. Acta 66, 3533–3547.

911   Enid Martinez, C., Mcbride, M.B., 1998. Coprecipitates of Cd, Cu, Pb and Zn in iron

912   oxides: Solid phase transformation and metal solubility after aging and thermal

913   treatment. Clays Clay Miner. 46, 537–545.

914   FracFocus Chemical Disclosure Registry, 2016. Ground Water Protection Council;

915   Interstate Oil & Gas Compact Commission; https://fracfocus.org

916   Furrer, G., Phillips, B.L., Ulrich, K.-U., Pöthig, R., Casey, W.H., 2002. The origin of

917   aluminum flocs in polluted streams. Science. 297, 2245–2247.

918   Golubev, S. V., Benezeth, P., Schott, J., Dandurand, J.L., Castillo, A., 2009. Siderite

919   dissolution kinetics in acidic aqueous solutions from 25 to 100°C and 0 to 50 atm

920   pCO$_2$. Chem. Geol. 260, 295–301.

921   Gouze, P., Luquot, L., 2011. X-ray microtomography characterization of porosity,

922   permeability and reactive surface changes during dissolution. J. Contam. Hydrol.

923   120–121, 45–55.

924   Haluszczak, L.O., Rose, A.W., Kump, L.R., 2013. Geochemical evaluation of flowback

925   brine from Marcellus gas wells in Pennsylvania, USA. Appl. Geochem. 28, 55–61.

926   Hammack, R.W., Harbert, W., Sharma, S., Stewart, B.W., Capo, R.C., Wall, A.J., Wells,

927   A., Diehl, R., Blaushild, D., Sams, J., Veloski, G., 2014. An evaluation of fracture

928   growth and gas/fluid migration as horizontal Marcellus Shale gas wells are

929   hydraulically fractured in Greene County, Pennsylvania. National Energy

930   Technology Laboratory: Pittsburgh, 2014; p 76.

931   Harrison, A.L., Dipple, G.M., Power, I.M., Mayer, K.U., 2016. The impact of evolving

932   mineral-water-gas interfacial areas on mineral-fluid reaction rates in unsaturated

933   porous media. Chem. Geol. 421, 65–80.

934   Harrison, A.L., Dipple, G.M., Power, I.M., Ulrich Mayer, K., 2015. Influence of surface

935   passivation and water content on mineral reactions in unsaturated porous media:

936   Implications for brucite carbonation and CO$_2$ sequestration. Geochim. Cosmochim.

937   Acta 148, 477–495.

938   Jambor, J.L., Dutrizac, J.E., 1998. Occurrence and constitution of natural and synthetic

939   ferrihydrite, a widespread iron oxyhydroxide. Chem. Rev. 98, 2549–2586.

940   Jennings, D.S., Antia, J., 2013. Petrographic characterization of the Eagle Ford shale,

941   South Texas: Mineralogy, common constituents, and distribution of nanometer-scale

942   pore types. *in*: W. Camp, E. Diaz, and B. Wawak, eds., Electron microscopy of shale

943   hydrocarbon reservoirs: AAPG Memoir 102, p. 101–113.

944   Jew, A.D., Dustin, M.K., Harrison, A.L., Joe-Wong, C.M., Thomas, D.L., Maher, K.M.,

945   Brown, G.E. Jr., Bargar, J.R., *in review*. Impact of organics and carbonates on the

946   oxidation and precipitation of iron during hydraulic fracturing of shale. Energy &

947   Fuels.

948   Jin, L., Mathur, R., Rother, G., Cole, D., Bazilevskaya, E., Williams, J., Carone, A.,

949   Brantley, S., 2013. Evolution of porosity and geochemistry in Marcellus Formation

950   black shale during weathering. Chem. Geol. 356, 50–63.

951   Johnston, J.H., Lewis, D.G., 1983. A detailed study of the transformation of ferrihydrite

952   to hematite in an aqueous medium at 92°C. Geochim. Cosmochim. Acta 47, 1823–

953   1831.

954   Jung, H.B., Um, W., Cantrell, K.J., 2013. Effect of oxygen co-injected with carbon

955   dioxide on Gothic shale caprock-CO_2-brine interaction during geologic carbon

956   sequestration. Chem. Geol. 354, 1–14.

957   Kerr, R.A., 2010. Natural gas from shale bursts onto the scence. Science. 328, 1624–

958   1626.

959   Law, B.E., Pollastro, R.M., Keighin, C.W., 1986. Geologic characterization of low-

960   permeability gas reservoirs in selected wells, greater Green River Basin, Wyoming,

961   Colorado, and Utah, *in*: AAPG Special Volumes: SG 24: Geology of Tight Gas

962   Reservoirs. pp. 253–169.

963   Lester, Y., Ferrer, I., Thurman, E.M., Sitterley, K.A., Korak, J.A., Aiken, G., Linden,

964   K.G., 2015. Characterization of hydraulic fracturing flowback water in Colorado:

965   Implications for water treatment. Sci. Total Environ. 512–513, 637–644.

966   Luquot, L., Andreani, M., Gouze, P., Camps, P., 2012. CO_2 percolation experiment

967   through chlorite/zeolite-rich sandstone (Pretty Hill Formation – Otway Basin–

968   Australia). Chem. Geol. 294–295, 75–88.

969   Luquot, L., Gouze, P., 2009. Experimental determination of porosity and permeability

970   changes induced by injection of CO_2 into carbonate rocks. Chem. Geol. 265, 148–

971   159.

972   Materials Data, Inc., 2002. Jade XRD Pattern Processing Ver. 6.5.

973   Michel, F.M., Barrón, V., Torrent, J., Morales, M.P., Serna, C.J., Boily, J.-F., Liu, Q.,

974   Ambrosini, A., Cismasu, a C., Brown, G.E., 2010. Ordered ferrimagnetic form of

975   ferrihydrite reveals links among structure, composition, and magnetism. Proc. Natl.

976   Acad. Sci. U.S.A. 107, 2787–2792.

977   Morel, F. M. M., J. G. Hering, 1993. Principles and applications

978   of aquatic chemistry. Wiley-Interscience, New York, 588 pp

979   Morgan, B., Lahav, O., 2007. The effect of pH on the kinetics of spontaneous Fe(II)

980   oxidation by O_2 in aqueous solution - basic principles and a simple heuristic

981   description. Chemosphere 68, 2080–2084.

982   Nicholson, R. V., Gillham, R.W., Reardon, E.J., 1990. Pyrite oxidation in carbonate-

983   buffered solution: 2. Rate control by oxide coatings. Geochim. Cosmochim. Acta 54,

984   395–402.

985   Nordstrom, D. K., 1982. Aqueous pyrite oxidation and the consequent formation of

986   secondary iron minerals. Acid sulfate weathering, 37-56.

987   Orem, W., Tatu, C., Varonka, M., Lerch, H., Bates, A., Engle, M., Crosby, L., McIntosh,

988   J., 2014. Organic substances in produced and formation water from unconventional

989   natural gas extraction in coal and shale. Int. J. Coal Geol. 126, 20–31.

990   Palandri J. L. and Kharaka Y. K. (2004) A compilation of rate parameters of water–

991   mineral interaction kinetics for application to geochemical modeling. US Geol. Sur.

992   Open File Rep. 2004-1068.

993   Parkhurst, D.L., Appelo, C.A.J., 2013. Description of input and examples for PHREEQC

994   Version 3 — A computer program for speciation , batch-reaction , one-dimensional

995   transport, and inverse geochemical calculations, in: U.S. Geological Survey

996   Techniques and Methods, Book 6, Chap. A43, 497 P. Denver, Colorado, p. 497.

997   Phan, T.T., Capo, R.C., Stewart, B.W., Graney, J.R., Johnson, J.D., Sharma, S., Toro, J.,

998   2015. Trace metal distribution and mobility in drill cuttings and produced waters

999   from Marcellus Shale gas extraction: Uranium, arsenic, barium. Appl. Geochem. 60,

1000   89–103.

1001   Phan, T.T., Capo, R.C., Stewart, B.W., Macpherson, G.L., Rowan, E.L., Hammack,

1002   R.W., 2016. Factors controlling Li concentration and isotopic composition in

1003   formation waters and host rocks of Marcellus Shale, Appalachian Basin. Chem.

1004   Geol. 420, 162–179.

1005   Pokrovsky, O.S., Golubev, S. V., Schott, J., 2005. Dissolution kinetics of calcite,

1006   dolomite and magnesite at 25 °C and 0 to 50 atm pCO_2. Chem. Geol. 217, 239–255.

1007   Renock, D., Landis, J.D., Sharma, M., 2016. Reductive weathering of black shale and

1008   release of barium during hydraulic fracturing. Appl. Geochem. 65, 73–86.

1009   Rimstidt, D.D., Vaughan, D.J., 2003. Pyrite oxidation: A state-of-the-art assessment of

1010   the reaction mechanism. Geochim. Cosmochim. Acta 67, 873–880.

1011 Rowan, E.L., Engle, M.A., Kraemer, T.F., Schroeder, K.T., Hammack, R.W., Doughten,

1012   M.W., 2015. Geochemical and isotopic evolution of water produced from Middle

1013   Devonian Marcellus shale gas wells, Appalachian basin, Pennsylvania. Am. Assoc.

1014   Pet. Geol. Bull. 99, 181–206.

1015 Roychaudhuri, B., Tsotsis, T.T., Jessen, K., 2013. An experimental investigation of

1016   spontaneous imbibition in gas shales. J. Pet. Sci. Eng. 111, 87–97.

1017 Schwertmann, U., Friedl, J., Stanjek, H., 1999. From Fe(III) ions to ferrihydrite and then

1018   to hematite. J. Colloid Interface Sci. 209, 215–223.

1019 Shih, J.-S., Saiers, J.E., Anisfeld, S.C., Chu, Z., Muehlenbachs, L.A., Olmstead, S.M.,

1020   2015. Characterization and analysis of liquid waste from Marcellus shale gas

1021   development. Environ. Sci. Technol. 49, 9557–9565.

1022 Smith, M.M., Wolery, T.J., Carroll, S.A., 2013. Kinetics of chlorite dissolution at

1023   elevated temperatures and CO_2 conditions. Chem. Geol. 347, 1–8.

1024 Steefel, C.I., Van Cappellen, P., 1990. A new kinetic approach to modeling water-rock

1025   interaction: The role of nucleation, precursors, and Ostwald ripening. Geochim.

1026   Cosmochim. Acta 54, 2657–2677.

1027 Stewart, B.W., Chapman, E.C., Capo, R.C., Johnson, J.D., Graney, J.R., Kirby, C.S.,

1028   Schroeder, K.T., 2015. Origin of brines, salts and carbonate from shales of the

1029   Marcellus Formation: Evidence from geochemical and Sr isotope study of

1030   sequentially extracted fluids. Appl. Geochem. 60, 78–88.

1031 Stringfellow, W.T., Domen, J.K., Camarillo, M.K., Sandelin, W.L., Borglin, S., 2014.

1032   Physical, chemical, and biological characteristics of compounds used in hydraulic

1033   fracturing. J. Hazard. Mater. 275, 37–54.

1034   Stumm, W., Lee, G.F., 1961. Oxygenation of ferrous iron. Ind. Eng. Chem. 53, 143–146.

1035   Tesoriero, A.J., Pankow, J.F., 1996. Solid solution partitioning of Sr^{2+}, Ba^{2+}, and Cd^{2+} to

1036   calcite. Science. 60, 1053–1063.

1037   Tuttle, M.L.W., Breit, G.N., Goldhaber, M.B., 2009. Weathering of the New Albany

1038   Shale, Kentucky: II. Redistribution of minor and trace elements. Appl. Geochem. 24,

1039   1565–1578.

1040   U.S Energy Information Administration, 2013. Technically recoverable shale oil and

1041   shale gas resources: An assessment of 137 shale formations in 41 countries outside

1042   the Unites States. EIA report: Washington, D.C., 2013; p 76.

1043   http://www.eia.gov/analysis/studies/worldshalegas/pdf/overview.pdf

1044   Vengosh, A., Jackson, R.B., Warner, N., Darrah, T.H., Kondash, A., 2014. A critical

1045   review of the risks to water resources from shale gas development and hydraulic

1046   fracturing in the United States. Environ. Sci. Technol. 16, 8334–8348.

1047   Vengosh, A., Warner, N., Jackson, R., Darrah, T., 2013. The effects of shale gas

1048   exploration and hydraulic fracturing on the quality of water resources in the United

1049   States. Procedia Earth Planet. Sci. 7, 863–866.

1050   Vidic, R.D., Brantley, S.L., Vandenbossche, J.M., Yoxtheimer, D., Abad, J.D., 2013.

1051   Impact of shale gas development on regional water quality. Science. 340, 1235009-

1052   1–1235009-9.

1053   Wang, L., Fortner, J.D., Giammar, D.E., 2015. Impact of water chemistry on element

1054   mobilization from Eagle Ford shale. Environ. Eng. Sci. 32, 310–320.

1055   Ziemkiewicz, P.F., Thomas He, Y., 2015. Evolution of water chemistry during Marcellus

1056   shale gas development: A case study in West Virginia. Chemosphere 134, 224–231.

1057 Zolfaghari, A., Dehghanpour, H., Noel, M., Bearinger, D., 2016. Laboratory and field

1058   analysis of flowback water from gas shales. J. Unconv. Oil Gas Resour. 14, 113–

1059   127.

1060

1061

1062 **Table 1. Initial chemical composition of shale samples[a]**

Element[b]	Barnett	Marcellus	Green River	Eagle Ford
Na (wt.%)	0.10	< 0.01	0.94	< 0.01
Mg (wt.%)	0.63	0.78	4.41	0.37
Al (wt.%)	7.29	10.50	2.66	5.82
Si (wt.%)	25.53	28.41	12.27	15.97
S (wt.%)	0.90	2.05	0.10	1.13
K (wt.%)	1.65	2.07	1.07	0.89
Ca (wt.%)	2.51	4.23	13.64	16.67
Fe (wt.%)	2.48	4.56	1.78	2.12
Ni (μg/g)	126.4	275.1	27.1	71.2
U (μg/g)	2.6	33.5	3.8	< 0.4
Pb (μg/g)	12.9	32.5	16.4	11.5
Sr (μg/g)	275.3	182.6	884.1	494.7
Mn (μg/g)	172.9	209.2	290.8	90.0
As (μg/g)	10.3	32.4	11.9	19.7

1063 [a]Data are from x-ray fluorescence analysis and are reproduced from Jew et al. (*in press*).
1064 [b]Uncertainty for triplicate measurements is $\leq$ 5%.

1065

1066 **Table 2. Initial mineralogical composition of shale samples based on x-ray**
1067 **diffraction analysis[a]**

Mineral (wt.%)[b]	Carbonate-poor		Carbonate-rich	
	Barnett	Marcellus	Green River	Eagle Ford
Quartz	44.2	42.2	31.4	25.2
Feldspars	4.9	3.7	8.0	nd[c]
Calcite	8.2	11.6	23.2	64.5
Dolomite	nd	1.1	28.9	nd
Pyrite	2.1	6.4	nd	2.7
Analcime	nd	nd	8.5	nd
Clays	40.6	35	nd	7.6

1068 [a]Data reproduced from Jew et al. (*in press*).
1069 [b]analytical uncertainty is $\leq$ 15 wt.%
1070 [c]nd = not detected

1071
1072
1073
1074

Figure Captions

1076

1077 **Figure 1.** Aqueous concentrations of (a) calcium, (b) pH, (c) iron, and (d) sulfate versus

1078 reaction time for all short-term experiments. Inset in (a) shows the percentage of total Ca

1079 remaining in the solid phase based on x-ray fluorescence spectroscopy of the initial solids

1080 and final aqueous Ca concentrations. The labels B, B2, M, EF, and GR represent the

1081 short-term Barnett, Barnett duplicate, Marcellus, Eagle Ford, and Green River

1082 experiments, respectively. Dashed lines in (c) represent calculated Fe concentrations

1083 based on measured SO_4^{2-} concentrations, assuming stoichiometric pyrite dissolution.

1084 Duplicate reactors are distinguished by filled versus unfilled symbols of the same type.

1085 Analytical error is smaller than symbol size unless otherwise shown.

1086

1087 **Figure 2.** Aqueous concentrations of (a) calcium, (b) pH, (c) iron, and (d) sulfate versus

1088 reaction time in all intermediate- and long-term experiments. Dashed and solid lines

1089 without symbols in (c) represent calculated Fe concentrations based on measured SO_4^{2-}

1090 concentrations, assuming stoichiometric pyrite dissolution. Line colors correspond to

1091 color coding for shale type as indicated in (a). Duplicate reactors are distinguished by

1092 filled versus unfilled symbols of the same type or different dash types for dashed lines.

1093 Analytical error is smaller than symbol size unless otherwise shown.

1094

1095 **Figure 3.** Silicon (a) and aluminum (b) concentrations versus reaction time in short-term

1096 experiments. Duplicate reactors are distinguished by filled versus unfilled symbols of the

1097 same type. Analytical error is smaller than symbol size unless otherwise shown. Silicon

1098   and aluminum mass balance (c) displayed as the percentage of total Si or Al remaining in

1099   the solid phase based on x-ray fluorescence spectroscopy of the initial solids and final

1100   aqueous Si and Al concentrations. Solid and striped bars represent Si and Al,

1101   respectively.

1102

1103   **Figure 4.** Saturation indices of secondary Fe(III)-bearing phases versus reaction time in

1104   the Marcellus (a) and Barnett (b) experiments of all durations. For clarity, only one of the

1105   Marcellus duplicates for the intermediate- and long-term experiments is shown. Orange,

1106   red, and black lines represent goethite [α-FeO(OH)], hematite [α-Fe$_2$O$_3$], and amorphous

1107   Fe(OH)$_3$, respectively. The solid grey line indicates chemical equilibrium with respect to

1108   a given solid phase (*i.e.* saturation index = 0).

1109

1110   **Figure 5.** Saturation index of calcite [CaCO$_3$] in all experiments. Data from the short-,

1111   intermediate-, and long-term experiments are represented by triangles, circles, and

1112   squares, respectively. Duplicate reactors are distinguished by filled versus unfilled

1113   symbols of the same type. The black dashed line indicates chemical equilibrium with

1114   respect to calcite (*i.e.* saturation index = 0).

1115

1116   **Figure 6.** Scanning electron micrographs of reacted versus unreacted shale samples.

1117   Barnett unreacted (a), Barnett reacted (b), Marcellus unreacted (c), Marcellus reacted (d),

1118   Green River unreacted (e), Green River reacted (f), Eagle Ford unreacted (g), and Eagle

1119   Ford reacted (h).

1120

1121 **Figure 7.** Aqueous Ni concentration versus time for the Barnett, Eagle Ford (EF), and

1122 Green River (GR) reactors of all durations (a). Aqueous Ni (b), Pb (c), and U (d)

1123 concentration versus time for Marcellus reactors of all durations. Duplicate reactors are

1124 distinguished by filled versus unfilled symbols of the same type. Analytical error is
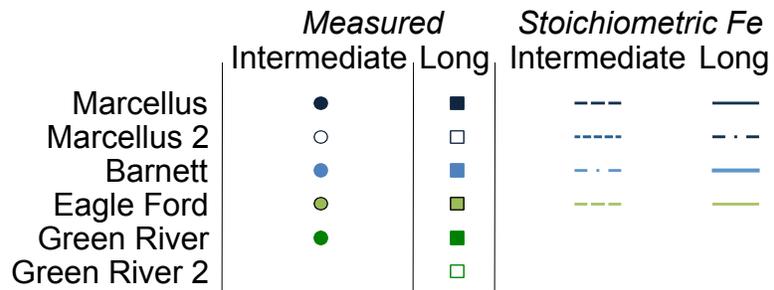
1125 smaller than symbol size unless otherwise shown.

1126

1127 **Figure 8.** Maximum measured aqueous Pb, U, and Ni concentrations versus maximum

1128 measured pH in Marcellus reactors of all durations (a). Analytical error is smaller than

1129 symbol size unless otherwise shown. Aqueous Fe to S molar ratios versus pH for all time

1130 points in Marcellus reactors of all durations (b). Duplicate reactors are distinguished by
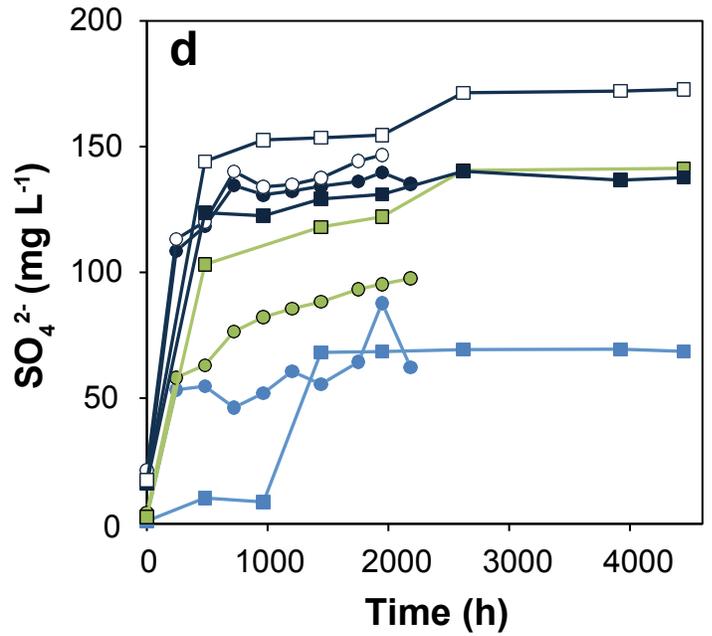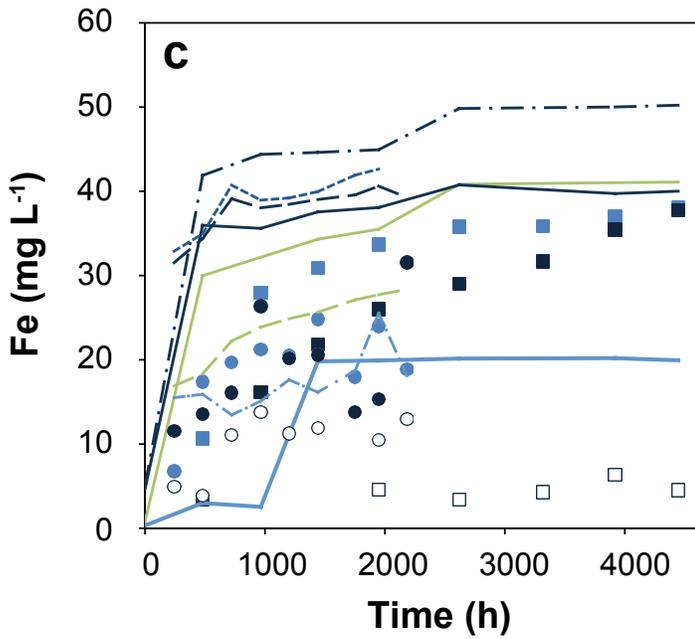
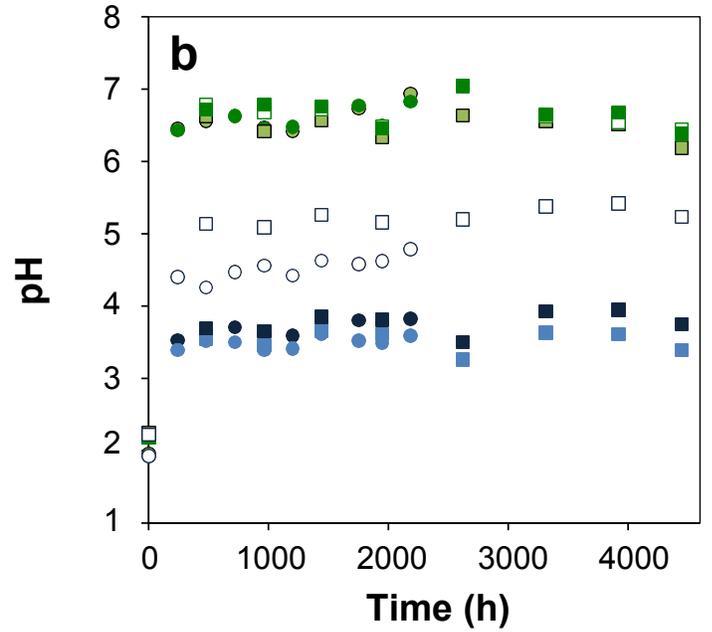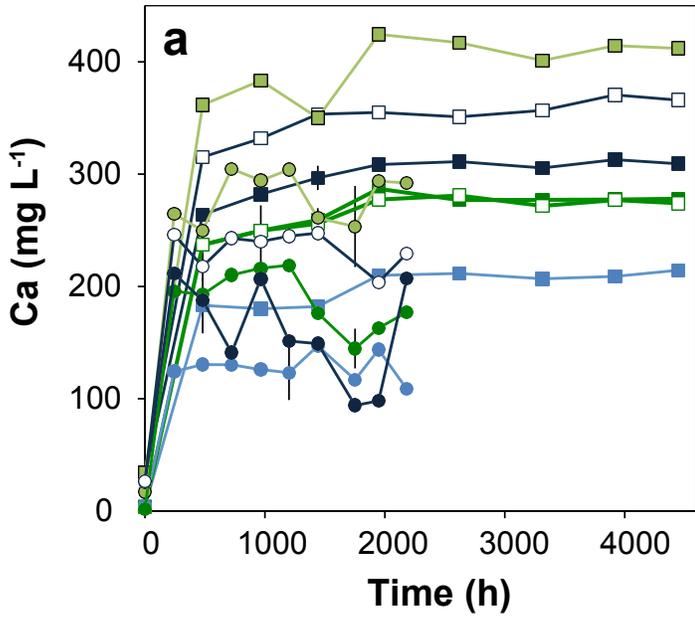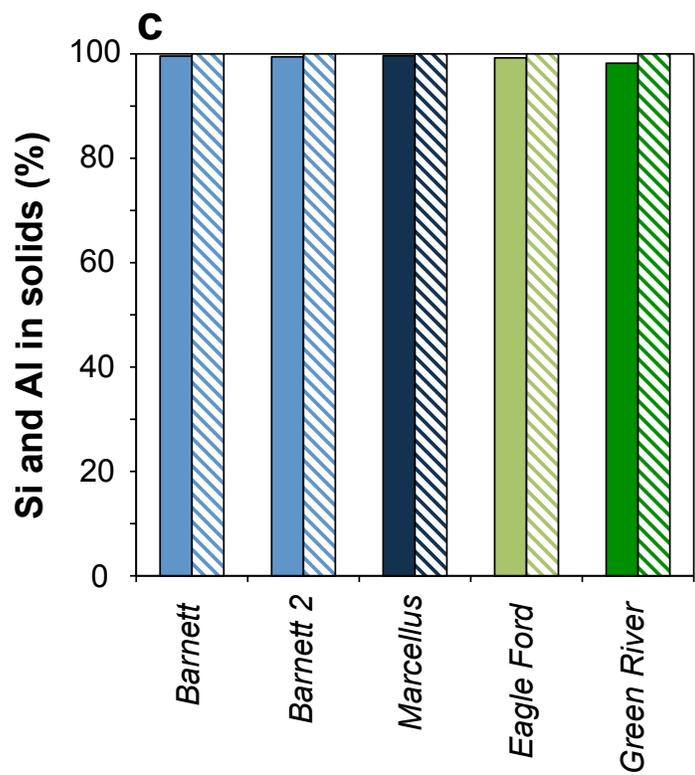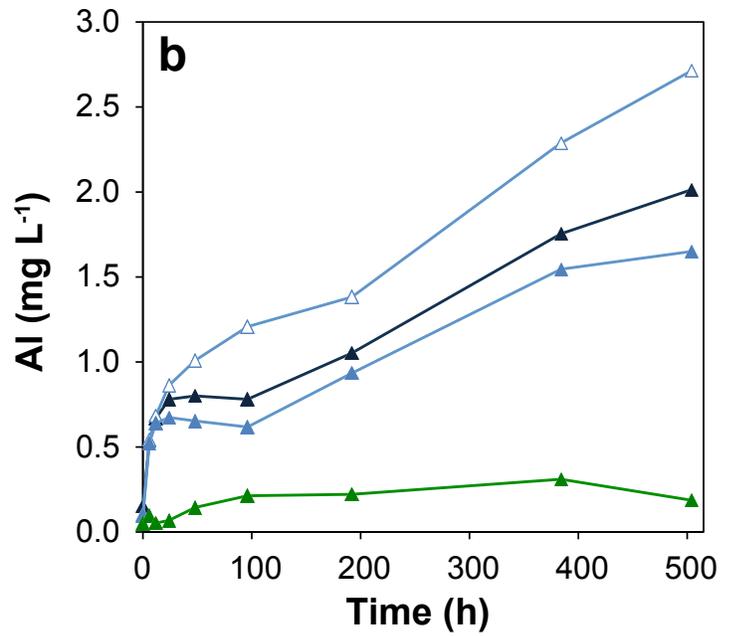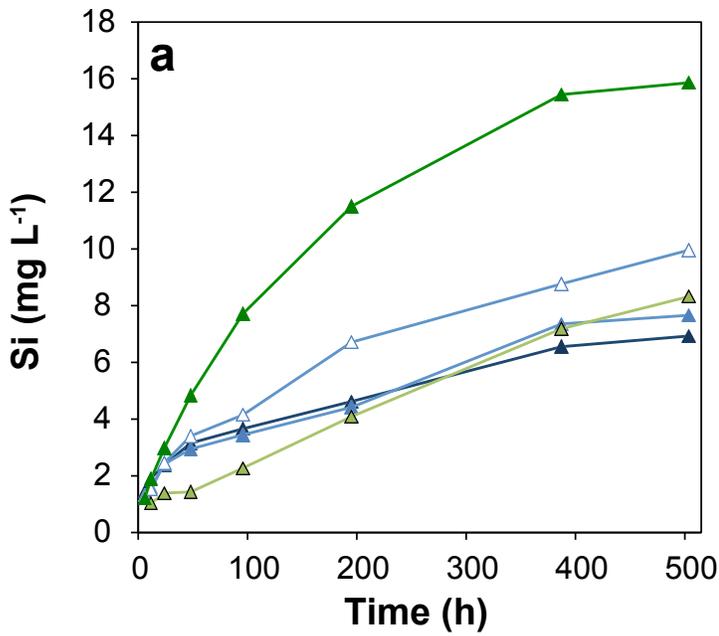1131 filled versus unfilled symbols of the same type.

1132

1133 **Figure 9.** Aqueous Sr concentration versus time in all reactors. Duplicate reactors are

1134 distinguished by filled versus unfilled symbols of the same type. Analytical error is

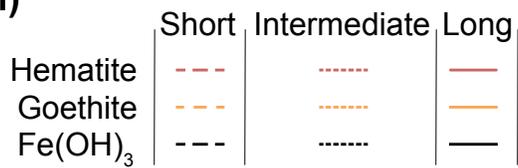1135 smaller than symbol size unless otherwise shown.

a

b

Carbonate-rich

Carbonate-poor

c

d
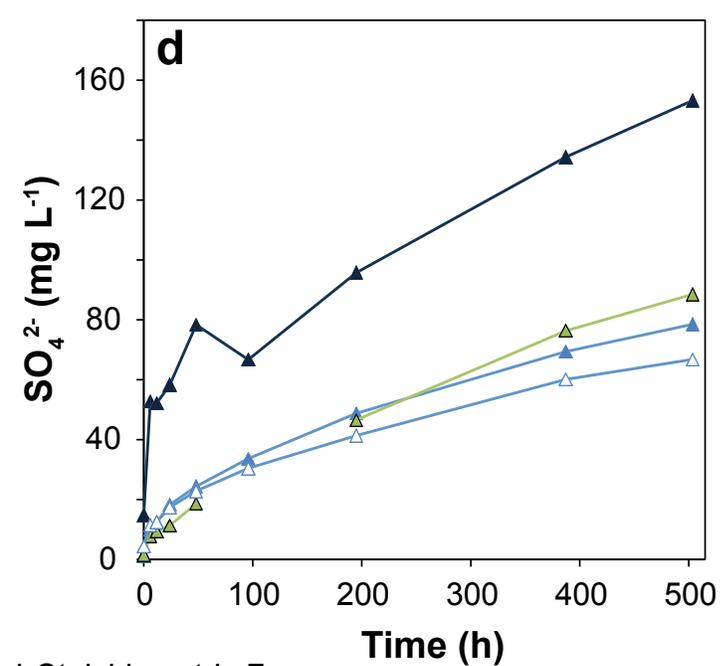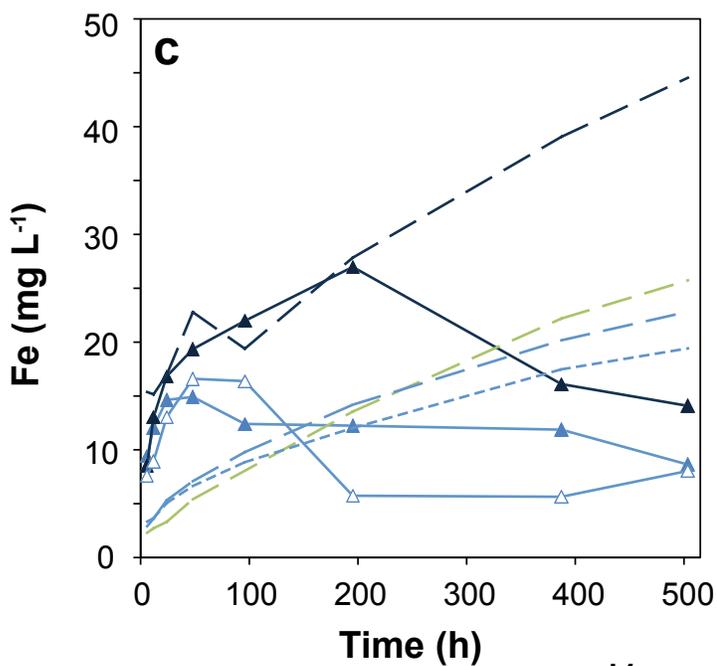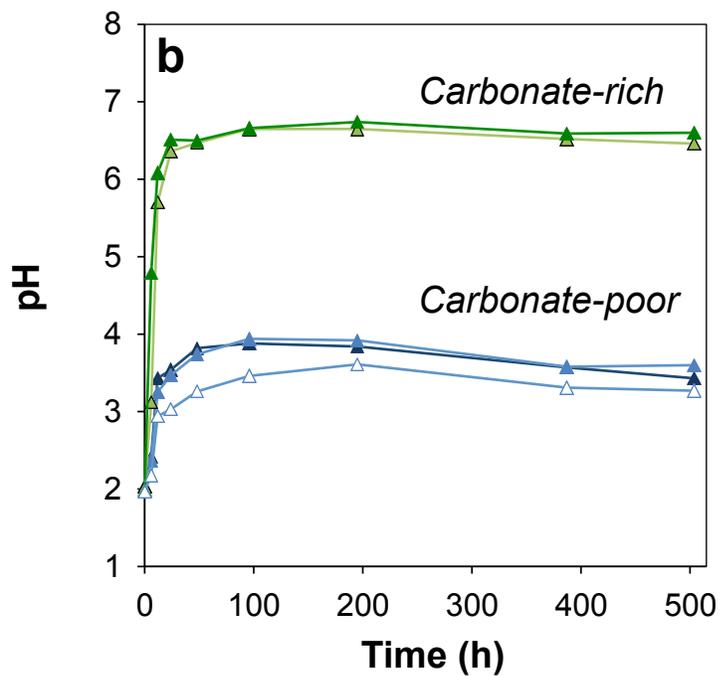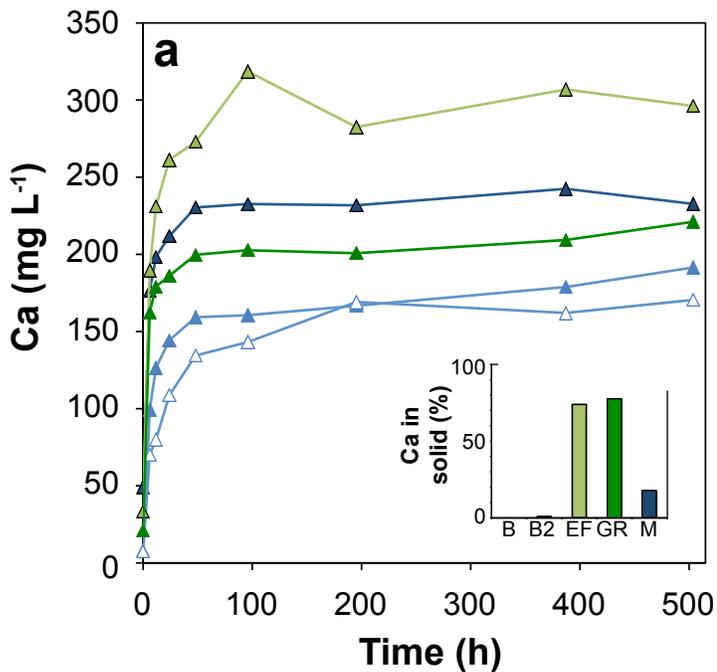
Measured	Stoichiometric Fe
Marcellus	
Barnett	
Barnett 2	
Eagle Ford	
Green River	

Figure legend:

Measured

	Intermediate	Long
Marcellus	●	■
Marcellus 2	○	□
Barnett	●	■
Eagle Ford	●	■
Green River	●	■
Green River 2		□

Stoichiometric Fe

	Intermediate	Long
Marcellus	– – –	——
Marcellus 2	········	–·–·–
Barnett	–·–·–	——
Eagle Ford	– – –	——

a

Si (mg L⁻¹)

b

Al (mg L⁻¹)

Time (h)

c

Si and Al in solids (%)

Barnett
Barnett 2
Marcellus
Eagle Ford
Green River

Si
Al

Marcellus
Barnett
Barnett 2
Eagle Ford
Green River

a) Marcellus

b) Barnett

	Short	Intermediate	Long
Hematite			
Goethite			
Fe(OH)$_3$			

a) Barnett unreacted

b) Barnett reacted

200 µm

200 µm

5 µm

c) Marcellus unreacted

d) Marcellus reacted

20 µm

20 µm

e) Green River unreacted

f) Green River reacted

20 µm

20 µm

g) Eagle Ford unreacted

h) Eagle Ford reacted

20 µm

5 µm

a

b

c

d

		Short	Intermediate	Long
Marcellus		▲	●	■
Marcellus 2			○	□
Barnett		▲	●	■
Barnett 2		△		

		Short	Intermediate	Long
Eagle Ford		▲	●	■
Green River		▲	●	■
Green River 2				□